

Relativistic Broadening of Iron Emission Lines in a Sample of AGN

Laura W. Brenneman¹, Christopher S. Reynolds²

ABSTRACT

We present a uniform X-ray spectral analysis of eight type-1 active galactic nuclei (AGN) that have been previously observed with relativistically broadened iron emission lines. Utilizing data from the *XMM-Newton* European Photon Imaging Camera (EPIC-pn) we carefully model the spectral continuum, taking complex intrinsic absorption and emission into account. We then proceed to model the broad Fe K α feature in each source with two different accretion disk emission line codes, as well as a self-consistent, ionized accretion disk spectrum convolved with relativistic smearing from the inner disk. Comparing the results, we show that relativistic blurring of the disk emission is required to explain the spectrum in most sources, even when one models the full reflection spectrum from the photoionized disk.

Subject headings: accretion, accretion disks – black hole physics – galaxies:nuclei – galaxies:Seyfert – X-rays:galaxies

1. Introduction

Black holes (BHs) are among the simplest objects in nature, able to be defined completely by mass, spin and charge alone. But whereas the mass of a BH is relatively straightforward to measure, provided material orbiting the BH can be observed (i.e., we are not blinded by the central engine), spin has proven much more challenging to constrain. With the advent of sensitive X-ray spectroscopy, allowing us to characterize processes very close to the BH in detail, we are now in a position to search for signatures of BH spin. This paper and its forthcoming counterpart (part II) represents the first survey to quantify the angular momenta of BHs in a sample of AGN using relativistically broadened iron lines as our spin

¹NASA's GSFC, mail code 662, Greenbelt MD 20771

²Dept. of Astronomy, University of Maryland, College Park, College Park MD 20742

diagnostic. Here, in Part I, we examine the statistical need for including relativistic effects when modeling the emission from the inner accretion disks around BHs.

As all current observables from a BH system are in one way or another related to the accretion process, any diagnostic of BH spin must be based on spin-induced changes to the accretion disk structure. BH spin manifests itself by setting the location of the innermost stable circular orbit (ISCO) which, in turn, sets the effective inner edge of a geometrically-thin accretion disk. For the purposes of this study, the “inner edge” of the disk is defined as the location inside of which no X-ray reflection signatures (e.g., iron line emission and Compton reflection hump) are produced either due to the disk becoming optically-thin or too highly ionized. As the magnitude of the (prograde) spin increases, frame-dragging stabilizes otherwise unstable orbits, causing the ISCO to move closer to the BH. The location of the inner edge of the disk can therefore be used to measure BH spin (e.g., Reynolds & Nowak 2003; Brenneman & Reynolds 2006; Reynolds & Fabian 2008).

The position of the ISCO can be constrained through detailed modeling of the X-ray spectrum of the disk. Two popular modeling schemes include fitting the thermal continuum of the disk (e.g., Narayan et al. 2007) and fitting the shape of the fluorescent Fe K line emitted by the disk in response to irradiation by the X-ray power-law (e.g., Brenneman & Reynolds 2006). The former method relies on *a priori* knowledge of the BH mass and distance as well as the disk inclination angle, however, and hence is most readily applied to Galactic BH systems (GBHs) in thermally dominant states as opposed to supermassive BHs found in the centers of AGN. By contrast, the shape of the iron line profile depends upon the gravitational redshift and fluid velocity field, both of which depend only upon the mass and radius of the black hole (M/R). Because the radius of the event horizon is directly dependent of the mass of the BH, the iron line profile is therefore mass-independent, making it a useful technique for deriving spin in any BH system (Reynolds & Nowak 2003). This is an especially useful technique in AGN in which the BH mass is often poorly constrained.

The shape of the iron line profile is determined by several physical parameters: the BH angular momentum, the radial extent of the disk, the emissivity profile of the disk and the inclination angle of the disk to the observer’s line of sight. A proper model for the iron line must also take into account the effects of the Doppler shift, Special Relativity (e.g., beaming) and General Relativity (e.g., gravitational redshift), each self-consistently calculated for the given value of BH spin. The two widely available relativistic line models within the XSPEC spectral analysis software were computed only for single values of spin; the `diskline` model describes only non-spinning Schwarzschild BHs (Fabian et al. 1989), and the `laor` model describes near-maximally ($a = 0.998$) Kerr BHs (Laor 1991). Thus, neither of these models allow for the self-consistent computation of a line profile from an arbitrary spin BH, even if

one allows the inner edge of the line emitting region to vary. If one wishes to constrain BH spin using self-consistent models, therefore, it is necessary to create a new, fully-relativistic model code which enables the BH spin to be fit as a free parameter.

We have developed such a model as both a line code (`kerrdisk`) and a convolution kernel (`kerrconv`) that can be applied to a full reflection spectrum expected from the disk.¹ To simplify the models, we have assumed that the BHs have no net charge (a very good approximation for all likely astrophysical BHs) and that there is a negligible amount of mass in the surrounding matter compared to the mass of the BH. Thus, the spacetime is described by the usual Kerr metric. These models were introduced and detailed in Brenneman & Reynolds (2006), hereafter BR06. BR06 also contains detailed comparisons of the `kerrdisk` and `kerrconv` models to similar codes developed by other groups (e.g., Dovčiak et al. 2004).

Our models assume that, in the co-moving frame of the disk surface, the emitted line/reflection spectrum is limb-darkened using the same prescription as Laor (1991). In fact, limb-darkening effects are usually completely unimportant to studies such as that conducted here; they only become significant for very high inclination angles, and furthermore it is only light-bending induced *differences* in the angle at which various parts of the disk are viewed that change the profile of the iron line.

BR06 also presents a series of model fits to the 330 ks *XMM-Newton*/EPIC-pn spectrum of the canonical broad iron line Sy 1 AGN MCG–6-30-15, noting that the best fit is achieved with a `kerrconv` model acting on an ionized disk reflection spectrum, where the inner edge of the disk was $r_{\min} \leq 1.62 r_g$. These data have allowed us to place formal constraints on the BH spin in MCG–6-30-15 of $a \geq 0.987$ (90% confidence level). Because this fit was performed under the assumption of a strict truncation of the iron line region at the innermost stable circular orbit (ISCO) in the disk, this constraint is somewhat weakened ($a \geq 0.92$) if the iron line emission region does in fact bleed inside of the ISCO (Reynolds & Fabian 2008). Given that MCG–6-30-15 harbors the broadest iron line in an AGN observed to date, this model fit reinforces our expectation that this AGN contains a BH of near-maximal spin. Many other, similar Sy 1 galaxies are also observed to have broad iron lines, however (Guainazzi et al. 2006; Nandra et al. 2007; Miller 2007), which begs two important questions: (1) can spectral observations of broad iron lines be used to robustly constrain BH spin, and (2) how is spin distributed between and among different types of BH systems?

To begin addressing these questions, we have collected a sample of eight other Sy 1 AGN from the *XMM-Newton* archive that have previously been observed to have broad iron lines.

¹These models are now available for public use in XSPEC12. Future updates will be made available initially at http://www.astro.umd.edu/~chris/kerrdisk/kerrdisk_model.html.

Using the same technique we used to model the spectrum of MCG–6-30-15 by first addressing the continuum and absorption and then considering the broad line region, we have assessed each AGN independently, with the initial goal of establishing whether we can definitively show that relativistic effects from the inner accretion disk are evident in these spectra (Part I, this paper). Following this conclusion, we will examine the archived *Suzaku* spectra of the AGN in our sample in order to take advantage of the increased spectral resolution and extended energy range that this observatory offers. The goal of this second study is to obtain statistically robust BH spin constraints whenever possible (Part II, forthcoming).

Section 2 of this work discusses the observations of the sources in our sample and the method used to reduce the EPIC-pn data and extract spectra. A summary of our modeling technique is given in §3. Section 4 contains the detailed spectral fitting results for each source. Results and tables comparing the relevant best-fit parameters for each source can be found in §5. Implications of these results, conclusions we have drawn and a prognosis for future work in this field are discussed in §6. Part II will discuss the *Suzaku* results and provide the first formal constraints on BH spin in our sample of AGN.

2. Observations and Data Reduction

Our source selection was based on work by Nandra et al. (2007) and the review by Miller (2007), both of whom consider the robustness of broad iron line detections across different source populations. The Miller review, in particular, collects all the recent X-ray data published on Seyfert sources and categorizes these objects by the strength and robustness of their broad iron line features. We have used these two studies as a guide for selecting the candidates for our sample, which we list in Table 1.

For this work, our data have been collected from the *XMM-Newton* Science Archive, using only publicly available observations. *XMM-Newton* data were preferentially used as opposed to *Chandra* data because of the superior collecting area of *XMM-Newton* in the 2–10 keV band where the broad Fe K α feature is the most prominent. There were insufficient numbers of publicly available *Suzaku* datasets at the time Part I of this study began (early 2007) to allow this work to be undertaken using *Suzaku*. The *Suzaku* study will be the focus of Part II in a forthcoming paper.

In this paper, we exclusively focus on the EPIC-pn data to avoid cross-calibration issues between the pn, MOS and RGS instruments. Though the RGS spectra in particular can provide detailed insight into the 0.3 – 2.0 keV spectrum and help illuminate the nature of the soft absorption and excess seen in so many Sy 1 AGN, the mismatch in resolution and

signal-to-noise as well as the possibility of cross-calibration errors severely reduce the utility of including RGS data in our formal spectral fitting. The basic parameters characterizing the observations of each of our sources are shown in Table 1.

For each source in question we performed reprocessing (when necessary) and data reduction with the SAS version 7.0.0 software, including the latest CCF calibration files. We have used the SAS `epatplot` task to compute the fraction of single, double, triple and quadruple events as a function of energy and compared these fractions to their nominal values as measured from weak source observations. For sources that are affected by pile-up, these fractions deviate from the nominal values due to the higher probability of wrong pattern classification. No significant deviation from the nominal single and double distributions was found for any of our sources, indicating that our EPIC-pn observations are not affected by pile-up. Source and background spectra and light curves were extracted using the `xmmselect` task from the SAS GUI. Response matrices and ancillary response files were generated using the `rmfgen` and `arfgen` tasks. These were then grouped with the spectral files using the FTOOLS package `grppha` with a minimum of 25 counts/bin in order to use χ^2 as a meaningful goodness-of-fit statistic. Spectral analysis was carried out as before for MCG–6-30-15 (BR06) with XSPEC version 12.4.0.

3. Spectral Analysis Methodology

In the following Section we outline the method used for the data reduction and spectral analysis of the AGN in our sample. We then discuss the spectral modeling of each source, culminating in a relativistically smeared ionized disk reflection spectrum model from which we infer the importance of taking GR into account when fitting each source. This is a critical first step toward measuring BH spin.

3.1. Continuum Fitting

We have endeavored to make the spectral analysis method as uniform as possible for all the AGN examined. There are, however, certain intrinsic physical differences between the sources that must be taken into account in order to properly model the continuum and isolate the iron line(s) in each case. Though all of our sources are Sy 1 AGN (or otherwise observed in states where they manifest broad disk lines), each system is unique in its physical properties. Some have higher signal-to-noise, either because of higher flux, longer observation time or both. Some exhibit evidence for complex, multi-zone warm absorbers (WAs) intrinsic

AGN	Date Obs.	Exposure (s)	Counts	pn Mode	Filter	RA (h)	Dec. (°)	z	Source Type
MCG-5-23-16	12/8/2005	121578	1.2×10^6	LW	Medium	9.7945	-30.7489	0.0085	Sy 1.9
Mrk 766	5/20/2001	111789	2.4×10^6	PSW	Medium	12.3074	29.8128	0.0129	Sy 1.5, NLS1
NGC 3783	12/19/2001	131025	1.6×10^6	PSW	Medium	11.6505	-37.7385	0.0097	Sy 1
NGC 4051	5/16/2001	121889	2.5×10^6	PSW	Medium	12.0527	44.5313	0.0023	Sy 1.5, NLS1
Fairall 9	7/5/2000	29209	2.0×10^5	PFW	Medium	1.3961	-58.8058	0.0470	Sy 1
Ark 120	8/24/2003	112130	2.3×10^6	PSW	Thin1	5.2699	-0.1502	0.0327	Sy 1
NGC 2992	5/19/2003	28917	3.4×10^5	PFW	Medium	9.7617	-14.3264	0.0077	Sy 1.9
3C 273	6/30/2004	19861	3.2×10^5	PSW	Thin1	12.4852	2.0524	0.1583	QSO, Sy 1

Table 1: Observation parameters for the eight AGN in our sample of broad iron line sources. Exposure times are after filtering, and counts are measured from 2 – 10 keV after filtering.

to the central engine, whereas some show only cold absorption from neutral hydrogen along our line of sight. A soft excess is seen in some sources but not others. And of course, the strength and breadth of the Fe $K\alpha$ line varies from source to source as well, though all have been chosen because they have previously shown evidence for broad iron lines.

In order to examine the iron line region in detail the continuum must first be accurately modeled. After excluding the energy ranges relevant to the iron line (4.0 – 8.0 keV) and the mirror edges ($\sim 1.5 - 2.5$ keV), we examine the rest of the 0.6 – 10.0 keV spectrum, fitting it with a power-law continuum typical of an AGN which is then modified by cold photoabsorption from neutral hydrogen. We set the minimum value of N_{H} equal to the Galactic column density along our line of sight to the source². If further absorption is necessary, we employ a second neutral absorber (either `zphabs` or `zpcfabs`) and allow the column (and covering fraction, if applicable) to vary as necessary to accommodate the cold absorption intrinsic to the system. Following the prior published analyses of these AGN, some sources require a second power-law component as well to properly model the basic continuum shape. We disregard energies below ~ 0.6 keV due to calibration uncertainties in this range for the EPIC-pn instrument.

If significant residual features remain after fitting this continuum model which indicate the presence of a soft excess and/or warm absorption, we include these components one by one as long as they make a significant difference in the global goodness-of-fit according to the F -test: $\Delta\chi^2 \leq -4$ for each new parameter introduced into the fit (Bevington 1969). The soft excess is typically parameterized by a blackbody component representing thermal emission in the central engine, but may also be modeled by bremsstrahlung emission or Comptonized emission from a thermal disk if either of these more complex forms gives a significantly better reduction in χ^2 . The warm absorption is modeled using the same XSTAR-generated multiplicative table model described in Brenneman et al. (2007) and BR06 in the analyses of NGC 4593 and MCG–6-30-15, respectively. Solar abundances are assumed for all elements and the redshift of the warm absorber(s) is set to that of the AGN host galaxy. Some AGN show no evidence for a warm absorber, while others statistically require up to two physically separate WA components, each exhibiting a distinct column density (N_{H}) and ionization parameter (ξ). We note that the EPIC-pn does not have sufficient spectral resolution to discern velocity differences between the warm absorber and the host galaxy; thus we do not need to include the warm absorber velocity as a free parameter.

²This parameter is determined from HI 21 cm surveys. See <http://heasarc.gsfc.nasa.gov/cgi-bin/Tools/w3nh/w3nh.pl> for the column density calculator as well as Dickey & Lockman (1990) and Kalberla et al. (2005).

Once the continuum has been properly modeled, we initially freeze the parameter values for all components except the power-law spectral index (Γ) and normalization (flux in $\text{ph cm}^{-2} \text{s}^{-1}$) and restrict our energy range from 2.5 – 10.0 keV in order to focus on the hard X-ray spectrum and the iron line region. Including the energies from 4.0 – 8.0 keV again, we check for residual emission (or absorption) lines from 6.4 – 6.97 keV, indicating the presence of unmodeled neutral and/or partly ionized Fe $K\alpha$ in the spectrum. Because these sources have been pre-determined to possess significant, broadened iron emission, it is not surprising that such residual emission features are seen in each case. We begin by attempting to fit the 6.4 keV line of neutral iron (and any other ionized iron lines) with a simple Gaussian feature, with the line width frozen at $\sigma = 0$ keV (i.e., intrinsically narrow) and the redshift again set to the cosmological value for the host galaxy. Such narrow lines are expected to originate from the outer accretion disk, or perhaps from reprocessing in a Compton-thick toroidal region surrounding the nucleus. As expected, in each case we note significant residual “wings” remaining around the Fe $K\alpha$ feature after this narrow core was fit, indicating the presence of a broad component to the line originating from closer to the BH.

3.2. Fitting the Iron Line Profile

To assess the robustness of the broad iron component and the importance of relativistic smearing in the spectrum, we follow our continuum fitting procedure (including modeling the narrow core of the iron line) by running each source through two additional steps of more complex modeling in the broad iron line region.

We begin by adding to the spectral model a broad iron line described by: (1) a broad Gaussian line (σ =free), replaced by (2) the `diskline` model (spin hardwired at $a = 0.0$), then replaced by (3) the `laor` model (spin hardwired at $a = 0.998$). The broad Gaussian is used primarily to gauge the energy and velocity width of the line in order to infer its radius of origin, whereas the relativistic line models are thought to be more physically accurate representations of the line morphology. The energy of the line is initially set to a rest-frame energy of 6.4 keV, corresponding to the energy of the cold Fe $K\alpha$ line. We use the change in χ^2/ν with the addition of the broad line component to verify whether a broad line is statistically warranted in our global model. According to this criterion, all of our sources required a broad line, and relativistic broadening was robustly preferred over a simple Gaussian in half of the cases. This is unsurprising since our objects were preselected to possess reported broad iron lines. Using the simple `diskline` and `laor` models, we also note the inner radius of disk emission: a broad line with the potential to diagnose BH spin

should have an inner disk radius of roughly $r_{\min} \leq 6 r_g$. We relax this restriction here to allow for differences in fit that may be achieved through different models, requiring that $r_{\min} \lesssim 20 r_g$ to infer that relativistic broadening is important.

We next perform a study to assess the degree to which the X-ray reflection continuum may be contaminating (or even mimicking) the broad iron line. To begin with, we replace the broad iron line with a *static* (unsmearing) ionized reflection spectrum (Ross & Fabian 2005) and refit. We then note the change in the goodness-of-fit criterion when the reflection spectrum is subjected to smearing characterizing a relativistic disk by convolving the spectrum with a line profile smearing kernel. The first such kernel we use is for a non-spinning BH ($a = 0.0$) and is known as `rdblur`. The second convolution model assumes a maximally-spinning BH ($a = 0.998$) and is known as `kdblur`.

We force the outer radius of disk emission to be $r_{\max} = 400 r_g$ in all the relativistic broad line fits. The value itself is somewhat arbitrary; as long as $\alpha \gtrsim 2$ (where α here denotes the emissivity index of the disk and the disk radiates as a function of radius: $r^{-\alpha}$), emission from this outer part of the disk is negligible, and we have already incorporated a separate narrow line core component whose width dictates an origin in the outer disk or torus region. For the ionized disk component, we begin with the assumptions of solar iron abundance and relative neutrality ($\text{Fe}/\text{solar} = 1$ and $\xi = 30 \text{ erg cm}^{-1} \text{ s}^{-1}$). We then relax these assumptions and allow these two parameters to fit freely, provided that reasonable statistical error bars can still be obtained for each parameter. We also note that all the models used above assume that the disk radiation is truncated at the ISCO; that is, that no contribution to the continuum or iron line profile originates from within this region.

4. Source-by-source Model Fitting

4.1. Target selection

As mentioned in the previous Section, we have selected the AGN for our sample primarily based on the research performed by other groups on the robustness of broad iron line observations in various AGN and the likelihood of being able to identify relativistic blurring effects in these sources using the iron line method (Nandra et al. 2007; Miller 2007). In particular, Miller (2007) discusses recent results from 30 Seyfert AGN in which relativistic disk lines have been detected and published, and divides those sources up into three “tiers” based on the nature and robustness of the detections. Many of the sources overlap with those presented in Nandra et al. Though we have examined observed spectra from all of the 9 AGN listed in Tier 1 (the most robust cases), NGC 3516 and NGC 4151 were not included

in our study due to their extremely complex soft spectra (Turner et al. 2005; Schurch et al. 2004). We did analyze the other 7 sources in full: 3C 120, MCG–6-30-15, MCG–5-23-16, NGC 2992, NGC 4051, NGC 3783 and Mrk 766. 3C 120 is not included in this work, however, as our spectral fitting results for this object were inconclusive in several ways due in part to a paucity of photons. We have also examined 3 other sources from Tier 3 that are mentioned prominently in Nandra et al. : Fairall 9, Ark 120 and 3C 273.

4.2. Source-by-source results

We present the best-fitting results of our spectral analysis for each source in its own subsection below. In many cases the `kdblur` and `rdblur` results were very similar, implying that little can be inferred about the spin of the BH in these AGN without more data. A more detailed comparison of all of our models is taken up in §5. Note that the reflection fractions quoted are not fitted values, but rather are estimates calculated for the purpose of comparison to other studies which may model disk reflection differently (e.g., with `pexrav` rather than `reflion`). We expand on this point in greater detail in §5. Detailed spectral fitting results for MCG–6-30-15 can be found in BR06 and are therefore not included herein.

A table of best-fit parameters for each source is included, as are figures representing the residual features left behind after initially fitting the spectrum with an absorbed power-law, the final best fit to the spectrum, and the best-fit model components for each object.

4.2.1. MCG–5-23-16

MCG–5-23-16 is a moderately absorbed Seyfert galaxy of intermediate type (Sy 1.9). It is relatively nearby at a redshift of $z = 0.0085$, and with a typical 2 – 10 keV flux of $F_{2-10} \sim 8 \times 10^{-11} \text{ erg cm}^{-2} \text{ s}^{-1}$ it is one of the brightest known Seyfert galaxies (Reeves et al. 2006). The source has been observed previously to have a soft excess below $\sim 1 \text{ keV}$ and an absorbing column of $N_{\text{H}} \sim 10^{22} \text{ cm}^{-2}$ (Dewangan et al. 2003; Balestra et al. 2004), and *ASCA* observations have indicated the presence of a broad Fe $K\alpha$ line of $EW \sim 200 \text{ eV}$ (Weaver et al. 1997, 1998). The line was successfully modeled with a narrow core at the rest-frame energy of 6.4 keV and a broad component superposed on it. This feature was modeled with similar success in the *XMM-Newton* observations of Dewangen et al. and Reeves et al. , as well as the *Suzaku* observation also published by these authors (Reeves et al. 2007).

In December 2005, MCG–5-23-16 was simultaneously observed with *XMM-Newton*, *Chandra*, *Suzaku* and *RXTE*. The *XMM-Newton* results are reported by Reeves et al. as well

as Braitto et al. , and our data reduction followed those works (Reeves et al. 2006; Braitto et al. 2006). The EPIC-pn instrument had a net exposure of 96 ks and returned $\sim 1.2 \times 10^6$ photons after filtering.

As suggested by Reeves et al. , a simple photoabsorbed power-law fit does not model the continuum well, especially below ~ 1 keV. Adding in a source of soft thermal emission also leaves prominent residuals and does not adequately account for the shape of the soft excess, so following the lead of Reeves et al. we have employed a two-power-law model (Reeves et al. 2006): one of the power-law components is affected only by Galactic photoabsorption ($N_{\text{H}} = 8 \times 10^{20} \text{ cm}^{-2}$ as per Reeves et al.), and hence leaves the AGN system effectively unscattered, while the other component is also subject to absorption intrinsic to the AGN, in this case with a fitted absorbing column density of $N_{\text{H}} = 1.19 \pm 0.01 \times 10^{22} \text{ cm}^{-2}$. This component also experiences scattering within the system. We set both power-law photon indices to be equal, indicating that the two power-law components originate from the same physical reservoir of photons (with $\Gamma = 1.66 \pm 0.01$). Calculating the ratio of the flux of the scattered power-law component to the unscattered power-law component (from 0.6 – 10.0 keV, fitting only the continuum) yielded an estimate of the optical depth of the scattering plasma. In this case $\tau = 7.37 \times 10^{-4} \text{ ph cm}^{-2} \text{ s}^{-1} / 1.98 \times 10^{-2} \text{ ph cm}^{-2} \text{ s}^{-1} \approx 0.04$, so the scattered fraction is low, implying that the electron plasma is optically thin. No evidence for spectral curvature due to the presence of a WA was found in this source.

The spectrum does show evidence for two prominent, narrow emission lines of iron $K\alpha$ and $K\beta$ (at $E_{K\alpha} = 6.40 \pm 0.01$ keV and $E_{K\beta} = 7.06^{+0.02}_{-0.01}$ keV, with $EW_{K\alpha} = 167^{+15}_{-13}$ eV and $EW_{K\beta} = 104^{+32}_{-30}$ eV, respectively), as well as three narrow absorption lines of intermediately ionized iron or nickel at $E_1 = 7.24^{+0.03}_{-0.04}$ keV, $E_2 = 7.48 \pm 0.04$ keV and $E_3 = 7.85^{+0.02}_{-0.05}$ keV ($EW_1 = -79^{+30}_{-29}$ eV, $EW_2 = -121^{+49}_{-50}$ eV, and $EW_3 = -143 \pm 43$ eV, respectively).

After successfully modeling the continuum and narrow line parameters for MCG–5-23-16, we restricted our attention to the hard spectrum (2.5 – 10.0 keV) and analyzed the broad line component of this source using the method outlined above in §3.2. The initial broad Gaussian fit implied that the broad line originates in neutral iron with $E = 6.34 \pm 0.02$ keV and $\sigma = 0.28 \pm 0.03$ keV. The width of the line suggests an origin within $d \sim 100 r_g$ of the BH. A `laor` line component fit the data marginally better than a `diskline`, with an improvement of $\Delta\chi^2/\Delta\nu = -145/-4$ in global goodness-of-fit over a model without a broad iron line component. Here, ν is the number of degrees of freedom in the fit, defined by the total number of spectral channels in the data minus the number of free model parameters, so a decrease in ν implies an increase in the number of free model parameters.

We determined that an ionized disk reflection spectrum convolved with `kdblur` provides the best model fit, though the inner disk radius could only be weakly constrained ($r_{\text{min}} \leq$

$63 r_g$). This prevents us from being able to place any meaningful constraints on the spin of the BH in this source with these data, in spite of the presence of relativistic broadening in the iron line profile. Note that eliminating soft energies from the fit removed the statistical need for a second, soft power-law in the fit. For a full listing of best-fit model parameters and error bars for MCG–5-23-16, see Table 2. The residual iron line feature, best-fit model and best-fit model components for the hard spectrum are shown in Fig. 1. The `diskline` and `laor` fits are shown in Table 10, while comparisons of the ionized disk reflection spectrum with and without relativistic smearing can be found in Table 11.

4.2.2. NGC 3783

NGC 3783 is a bright, nearby Sy 1 galaxy at a redshift of $z = 0.0097$. It was first detected in X-rays with the *Ariel-V* all-sky survey (McHardy et al. 1981) and subsequently in the high Galactic latitude survey conducted by *HEAO-1* (Piccinotti et al. 1982). Since these early detections, there have been many observations of NGC 3783 with higher resolution instruments: A *ROSAT* observation of the source showed evidence of an ionized absorber in the soft band (Turner et al. 1993), which was confirmed during *ASCA* observations (George et al. 1995, 1998). High-resolution grating observations of NGC 3783 with *Chandra* and *XMM-Newton* followed, unveiling the soft spectrum of this source in detail (Kaspi et al. 2000, 2001, 2002; Blustin et al. 2002; Behar et al. 2003). The higher signal-to-noise of *XMM-Newton*, in particular, has also enabled the iron line to be studied extensively in this source (Reeves et al. 2004). Using two observations from December 2001, Reeves et al. have obtained ~ 240 ks of data on NGC 3783. Their global fits to the merged EPIC-pn spectrum are currently second in length only to the ~ 330 ks observation of MCG–6-30-15 (Fabian et al. 2002). In these observations, the source has an average 2 – 10 keV flux of $F_{2-10} = 6.8 \times 10^{-11} \text{ erg cm}^{-2} \text{ s}^{-1}$. The spectrum is noted to have iron line peaks at 6.39 ± 0.01 keV and 7.00 ± 0.02 keV, representing neutral Fe K α ($EW = 123 \pm 6$ eV) and a blend of ionized Fe K α and Fe K β ($EW = 34 \pm 5$ eV), respectively. A strong absorption line of intermediately ionized iron is also observed at 6.67 ± 0.04 keV ($EW = 17 \pm 5$ eV) that exhibits variability in direct correlation with that of the continuum flux. A weak red wing of the 6.39 keV line is noted by the authors, but once warm absorption is taken into account in the system the requirements for a broad Fe K α component are significantly reduced (Reeves et al. 2004).

We analyzed the first of the two December 2001 *XMM-Newton* observations. We chose not to merge the event files of both data sets to avoid the uncertainties inherent in so doing, instead focusing on only one data set with an effective exposure time of ~ 120 ks and a

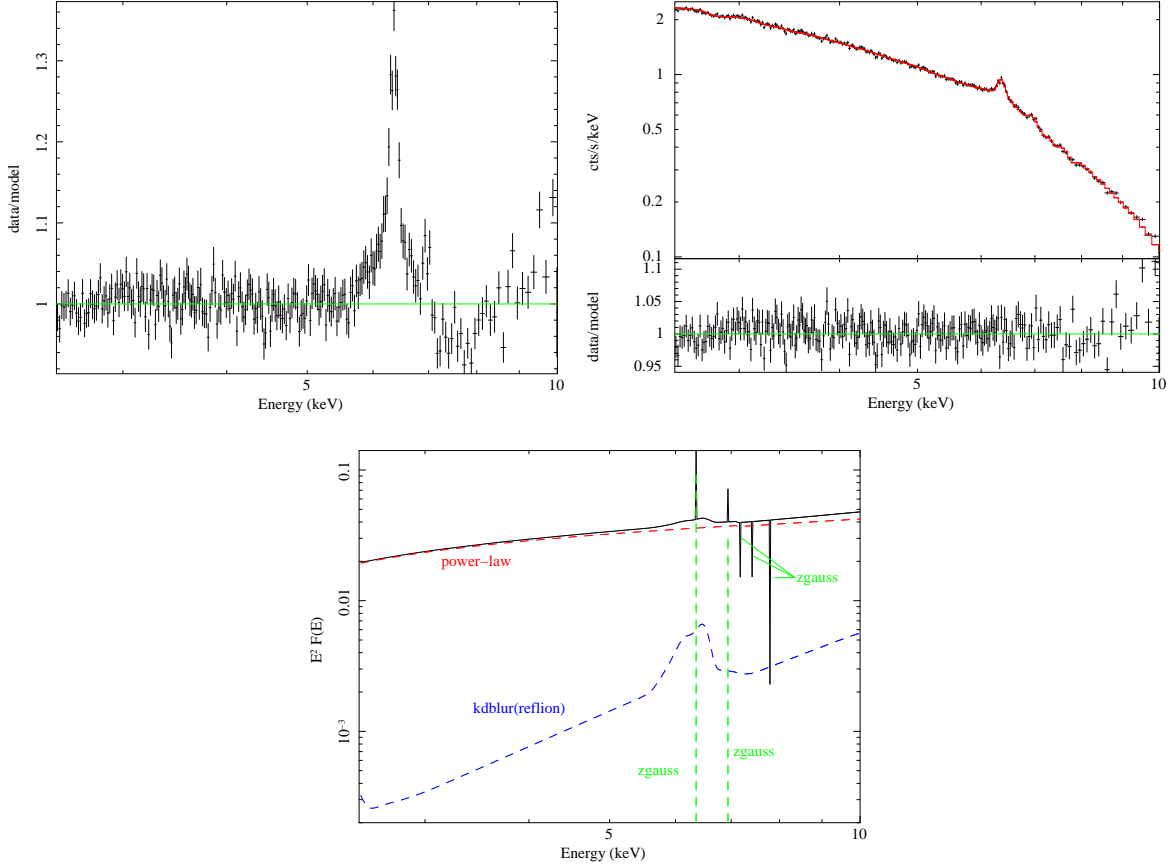


Fig. 1.— *Top left:* The 2.5 – 10.0 keV spectrum of MCG–5-23-16 fit with a two-power-law model modified by Galactic photoabsorption; data-to-model ratio. Note the prominent Fe K line and the large residual emission component above 7 keV, which likely indicates the presence of ionized disk reflection. $\chi^2/\nu = 2675/1499$ (1.78). *Top right:* Best-fit model for MCG–5-23-16, including our continuum model, two narrow emission lines, and three narrow absorption lines as well as an ionized disk reflection spectrum convolved with our `kdblur` relativistic smearing kernel. $\chi^2/\nu = 1485/1488$ (1.00). *Bottom:* An $E^2 F(E)$ plot depicting the relative flux in each of the best-fit model components in the spectrum.

Model Component	Parameter	Value
phabs	$N_{\text{H1}} (\text{cm}^{-2})$	8×10^{20}
zphabs	$N_{\text{H2}} (\text{cm}^{-2})$	$1.19^{+0.01}_{-0.01} \times 10^{20}$
zpo	Γ_{po} flux ($\text{ph cm}^{-2} \text{s}^{-1}$)	$1.66^{+0.01}_{-0.01}$ $1.98^{+0.04}_{-0.13} \times 10^{-2}$
zpo	Γ_{po} flux ($\text{ph cm}^{-2} \text{s}^{-1}$)	$1.66^{+0.01}_{-0.01}$ $7.37^{+0.09}_{-0.21} \times 10^{-4}$
zgauss	E (keV) flux ($\text{ph cm}^{-2} \text{s}^{-1}$) EW (eV)	$6.40^{+0.01}_{-0.01}$ $4.00^{+0.35}_{-0.32} \times 10^{-5}$ 167^{+15}_{-13}
zgauss	E (keV) flux ($\text{ph cm}^{-2} \text{s}^{-1}$) EW (eV)	$7.06^{+0.02}_{-0.01}$ $9.80^{+2.98}_{-2.87} \times 10^{-6}$ 104^{+32}_{-30}
zgauss	E (keV) flux ($\text{ph cm}^{-2} \text{s}^{-1}$) EW (eV)	$7.24^{+0.03}_{-0.04}$ $-7.39^{+2.84}_{-2.73} \times 10^{-6}$ -79^{+30}_{-29}
zgauss	E (keV) flux ($\text{ph cm}^{-2} \text{s}^{-1}$) EW (eV)	$7.48^{+0.04}_{-0.04}$ $-6.93^{+2.83}_{-2.84} \times 10^{-6}$ -121^{+49}_{-50}
zgauss	E (keV) flux ($\text{ph cm}^{-2} \text{s}^{-1}$) EW (eV)	$7.85^{+0.02}_{-0.05}$ $-9.62^{+2.90}_{-2.86} \times 10^{-6}$ -143^{+43}_{-43}
kdblur	α i ($^{\circ}$) $r_{\text{min}} (r_{\text{g}})$ $r_{\text{max}} (r_{\text{g}})$	$2.38^{+2.02}_{-1.33}$ 28^{+9}_{-6} 33^{+31}_{-33} 400
reflion	Fe/solar $\xi_{\text{refl}} (\text{erg cm}^{-1} \text{s}^{-1})$ Γ_{refl} R_{refl} flux ($\text{ph cm}^{-2} \text{s}^{-1}$)	$0.61^{+0.08}_{-0.05}$ 30^{+1}_{-0} $1.66^{+0.01}_{-0.01}$ $0.41^{+0.02}_{-0.02}$ $1.64^{+0.10}_{-0.10} \times 10^{-5}$
χ^2/ν		1485/1488 (1.00)

Table 2: Best-fitting model parameters for the 2.5 – 10.0 keV spectrum of MCG–5-23-16, including components and parameter values from 0.6–1.5 keV for completeness. The energies from 1.5–2.5 keV were not included due to the presence of absorption edges from the *XMM-Newton* mirrors. Error bars are quoted at 90% confidence. For the **zgauss** lines, we required each to be intrinsically narrow, i.e., $\sigma = 0$ keV. Redshifts were frozen at the cosmological value for the source, in this case $z = 0.0085$. Note the absence of warm absorption and a soft excess in this object. When no error bars are quoted, the parameter in question is frozen at the given value.

total of $\sim 1.6 \times 10^6$ photons after filtering. This number of counts is still large enough to obtain valid statistical fits to the model parameters used. We follow the data reduction steps of Reeves et al., excluding the last part of the observation due to contamination from a background flare. Our analysis follows in the same spirit as these authors, but in order to remain consistent with the method described above in §3 we do not make any assumptions about the soft spectrum and continuum emission based on prior RGS results (Blustin et al. 2002).

We began our analysis of the time-averaged spectrum with a simple photoabsorbed power-law fit using the Galactic absorbing column of $N_{\text{H}} = 8.5 \times 10^{20} \text{ cm}^{-2}$, and neglecting the energy ranges associated with the mirror edges and the iron lines, as in §3. This fit leaves obvious residuals in all parts of the spectrum, however, and is especially poor for the soft energies below $\sim 1.5 \text{ keV}$. Continuum curvature associated with a soft excess and warm absorption are both clearly evident. As discussed by Reeves et al., the fit was much improved with the addition of a thermal blackbody component ($kT \sim 0.07 \pm 0.01 \text{ keV}$, as compared with their value: $kT \sim 0.09 \pm 0.01 \text{ keV}$). We approached the question of the warm absorption in the same manner as Reeves et al., using our XSTAR table model to parameterize the column density and ionization level of the absorbing medium. As with these authors, we found statistical evidence for a multi-zone warm absorption structure, though our fitted values for the column densities and ionization parameters of these zones vary from those of Reeves et al. These authors find $N_{\text{H1}} = 1.1 \times 10^{21} \text{ cm}^{-2}$ and $\log \xi_1 = -0.1$ (for this zone, Fe/solar = 10, in contrast to the other zones with solar iron abundance), $N_{\text{H2}} = 1.2 \times 10^{22} \text{ cm}^{-2}$ and $\log \xi_2 = 2.1$, with $N_{\text{H3}} = 4.4 \times 10^{22} \text{ cm}^{-2}$ and $\log \xi_3 = 3.0$ (no final error bars were given). By contrast, we find $N_{\text{H1}} = 1.80^{+0.23}_{-0.29} \times 10^{20} \text{ cm}^{-2}$ and $\log \xi_1 = 0$, $N_{\text{H2}} = 1.58^{+0.65}_{-0.62} \times 10^{23} \text{ cm}^{-2}$ and $\log \xi_2 = 2.82 \pm 0.94$, with $N_{\text{H3}} = 8.43^{+0.07}_{-0.25} \times 10^{23} \text{ cm}^{-2}$ and $\log \xi_3 = 3.79^{+0.02}_{-0.14}$. As with the results of Reeves et al. the third, neutral absorber of smaller column density was required to obtain a quality fit, but a very high iron abundance was necessary: Fe/solar = 10, where the abundance was approximated iteratively and held constant in the final fit because it was at the endpoint of its parameter space. We used the same technique to constrain the ionization parameter of this absorbing zone for the same reason. The differences between our results and those of Reeves et al. are not surprising, however, because Reeves et al. base their fits on the RGS results for this source (Blustin et al. 2002). We do not use any *a priori* information to augment or guide the EPIC-pn spectral fits due to calibration uncertainties. Finally, we allowed for a second neutral hydrogen absorbing column intrinsic to the source (using the `zpcfabs` model component) in an effort to improve the goodness-of-fit and found that the spectrum preferred a higher value than the Galactic column: $N_{\text{H}} = 2.77^{+0.11}_{-0.13} \times 10^{21} \text{ cm}^{-2}$ with a covering fraction of $f = 87 \pm 2\%$. This was also in contrast to the Reeves et al. result, where the cold hydrogen column was held at the Galactic value and no intrinsic neutral hydrogen

absorption was allowed. The differences in absorbing structures between our model and that of Reeves et al. also explain the difference in photon indices of the power-law continuum in the two models: our best-fit value was marginally softer, at $\Gamma = 1.83_{-0.04}^{+0.03}$, whereas Reeves et al. found a harder photon index of $\Gamma = 1.73 \pm 0.01$.

Reeves et al. found two emission peaks in the spectrum at 6.39 ± 0.01 keV ($EW = 123 \pm 4$ eV) and 7.00 ± 0.02 keV ($EW = 34 \pm 5$ eV), representing cold Fe K α and likely a blend of ionized Fe K α and Fe K β , respectively. The latter line, in particular, showed no appreciable variance over the observation, leading the authors to postulate a relatively distant origin for the lines away from the central parts of the accretion disk. A 6.67 ± 0.04 keV absorption feature ($EW = 17 \pm 5$ eV) of highly ionized iron was also seen which did appear to vary with time and was strongest when the continuum flux was highest, suggesting an origin in the region of the warm absorber within 0.1 parsec of the nucleus. Though inclusion of the WA structure (tailored to include this absorption feature) did lessen the statistical case for a broad iron line in NGC 3783, Reeves et al. nonetheless identified a residual broad feature which they fit using a `diskline` model with $\alpha = 3.3 \pm 0.5$, $i = 19 \pm 9^\circ$, $r_{\min} = 6.0 r_g$ (held constant, with $r_{\max} = 100 r_g$), and $EW = 58 \pm 12$ eV.

We also detected the emission and absorption features discussed by Reeves et al., though we found that the equivalent widths for the Fe K α and Fe K α /K β blend differed from the fits performed by these authors: $EW_{K\alpha} = 65 \pm 12$ eV, $EW_{K\alpha/K\beta} = 28 \pm 3$ eV. As mentioned above, the inclusion of the three-zone WA structure eliminated the need to include a separate Gaussian absorption line at 6.67 keV. It should also be noted that, contrary to the Reeves et al. analysis, we required the core of the 6.4 keV line to be intrinsically narrow, so it is not unusual that we obtain a smaller equivalent width than Reeves et al. When we included a broad `diskline` component of the neutral K α line, the goodness-of-fit improved dramatically: $\Delta\chi^2/\Delta\nu = -170/-4$. This fit proved superior to both a `laor` line model and a broad Gaussian component, the latter of which particularly did not model the shape of the line well. Our best fit to the hard spectrum of NGC 3783 convolved an ionized disk reflection spectrum with `rdblur`, as can be seen in Table 3 below. The inclusion of the ionized disk reflection spectrum component (`reflion`) accounted for the soft excess self-consistently, without the need to include the phenomenological blackbody component. Adding in the effects of relativistic smearing on this reflection spectrum, our constraints on the radial extent of the disk showed that $r_{\min} \leq 46 r_g$, making it difficult to distinguish a rapidly-spinning BH from a slowly-spinning one, even though relativistic disk effects are clearly important in broadening the iron line profile. The residual iron line feature, best-fit model and best-fit model components for the hard spectrum are shown in Fig. 2. The `diskline` and `laor` fits are shown in Table 10, while comparisons of the ionized disk reflection spectrum with and without relativistic smearing can be found in Table 11.

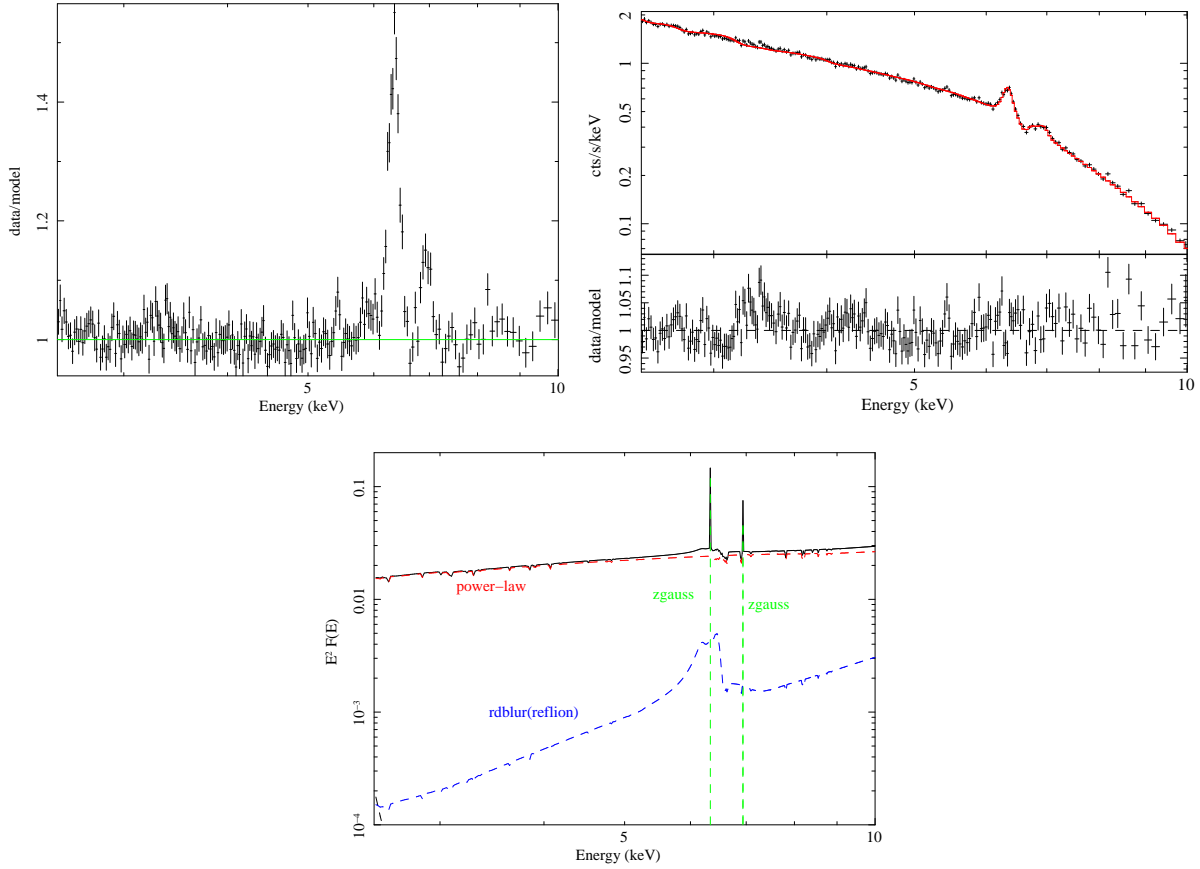


Fig. 2.— *Top left:* The 2.5 – 10.0 keV spectrum of NGC 3783 fit with a power-law model modified by Galactic photoabsorption, along with a three-zone warm absorber and a black-body soft excess. $\chi^2/\nu = 2751/1487$ (1.85). *Top right:* The 2.5 – 10.0 keV best-fit model for NGC 3783, including our continuum model and two narrow emission lines as well as an ionized disk reflection spectrum convolved with the `rdblur` relativistic smearing kernel. $\chi^2/\nu = 1480/1487$ (1.00). *Bottom:* An $E^2 F(E)$ plot depicting the relative flux in each of the best-fit model components in the spectrum.

Model Component	Parameter	Value
phabs	$N_{\text{H}} (\text{cm}^{-2})$	8.50×10^{20}
zpcfabs	$N_{\text{H}2} (\text{cm}^{-2})$	$2.77^{+0.11}_{-0.13} \times 10^{21}$
	$f_{\text{cov}} (\%)$	88^{+2}_{-2}
WA 1	$N_{\text{WA1}} (\text{cm}^{-2})$	$1.80^{+0.23}_{-0.29} \times 10^{20}$
	$\log \xi_{\text{WA1}}$	0
WA 2	$N_{\text{WA2}} (\text{cm}^{-2})$	$1.58^{+0.65}_{-0.62} \times 10^{23}$
	$\log \xi_{\text{WA2}}$	$2.82^{+0.94}_{-0.94}$
WA 3	$N_{\text{WA3}} (\text{cm}^{-2})$	$8.43^{+0.07}_{-0.25} \times 10^{23}$
	$\log \xi_{\text{WA3}}$	$3.79^{+0.02}_{-0.14}$
zpo	Γ_{po}	$1.83^{+0.03}_{-0.04}$
	flux ($\text{ph cm}^{-2} \text{s}^{-1}$)	$1.33^{+0.05}_{-0.05} \times 10^{-4}$
zgauss	E (keV)	$6.40^{+0.02}_{-0.01}$
	flux ($\text{ph cm}^{-2} \text{s}^{-1}$)	$3.25^{+0.37}_{-0.37} \times 10^{-7}$
	EW (eV)	65^{+7}_{-7}
zgauss	E (keV)	$7.01^{+0.02}_{-0.03}$
	flux ($\text{ph cm}^{-2} \text{s}^{-1}$)	$1.11^{+0.20}_{-0.20} \times 10^{-7}$
	EW (eV)	28^{+5}_{-5}
rdblur	α	$1.90^{+1.40}_{-0.87}$
	i ($^{\circ}$)	23^{+3}_{-3}
	$r_{\text{min}} (r_{\text{g}})$	17^{+29}_{-17}
	$r_{\text{max}} (r_{\text{g}})$	400
reflion	Fe/solar	$0.83^{+0.12}_{-0.88}$
	$\xi_{\text{refl}} (\text{erg cm}^{-1} \text{s}^{-1})$	30^{+24}_{-0}
	Γ_{refl}	$1.83^{+0.03}_{-0.04}$
	R_{refl}	$0.49^{+0.22}_{-0.37}$
	flux ($\text{ph cm}^{-2} \text{s}^{-1}$)	$7.46^{+2.88}_{-4.07} \times 10^{-8}$
χ^2/ν		1480/1487 (1.00)

Table 3: Best-fitting model parameters for the 2.5–10.0 keV spectrum of NGC 3783, including components and parameter values from 0.6 – 1.5 keV for completeness. The energies from 1.5 – 2.5 keV were not included due to the presence of absorption edges from the *XMM-Newton* mirrors. Error bars are quoted at 90% confidence. For the **zgauss** lines, we required each to be intrinsically narrow, i.e., $\sigma = 0$ keV. Redshifts were frozen at the cosmological value for the source, in this case $z = 0.0097$. Note the multi-zone warm absorber present in this object, similar to many other Sy 1 sources.

4.2.3. Mrk 766

Mrk 766 is designated as a classic, bright NLS1 galaxy (Sy 1.5) with a redshift of $z = 0.0129$ and a typical 2 – 10 keV flux of $F_{2-10} \sim 2.5 \times 10^{-11} \text{ erg cm}^{-2} \text{ s}^{-1}$ (Pounds et al. 2003). Previous X-ray observations of this source have provided contradictory evidence on the detection of a broad Fe K α feature. Although not one of the most convincing cases, Mrk 766 was included in an *ASCA* spectral survey of bright Seyfert galaxies showing evidence of relativistic iron lines (Nandra et al. 1997). A separate analysis of simultaneous *ROSAT* and *ASCA* observations (Leighly et al. 1996), however, showed the X-ray spectrum to be described by a power-law of index increasing strongly with flux from $\Gamma \sim 1.6$, but with only a narrow Fe K α emission line ($EW \sim 100 \text{ eV}$ at 6.4 keV). A later observation with *BeppoSAX* found a steeper power-law ($\Gamma \sim 2.2$), and evidence for an absorption edge at $\sim 7.4 \text{ keV}$ (Matt et al. 2000), implying strong reflection from intermediately ionized material. Interestingly, based on *XMM-Newton* observations of the source, Turner et al. found that energy-time maps of Mrk 766 reveal a periodic energy shift in an ionized component of Fe K α emission, with a period of $\sim 165 \text{ ks}$. This can be interpreted as evidence for emission from orbiting gas within $\sim 100 r_g$ of the central BH. A likely explanation is that this gas represents a hot spot on the disk illuminated by magnetic reconnection (Turner et al. 2006).

We examine the May 2001 *XMM-Newton* observation of Mrk 766 taken by Mason et al., from which the RGS results were published in 2003 (Mason et al. 2003) and the EPIC spectra were explored more thoroughly by other authors (Pounds et al. 2003; Turner et al. 2006). In our re-analysis, the EPIC-pn data have an effective exposure time of 128 ks and the filtered data yield $\sim 2.4 \times 10^6$ photons.

Mrk 766 bears many spectral similarities to MCG–6–30–15, showing significant complexity beyond a simple photoabsorbed power-law fit. There is clear evidence for a thermal soft excess below $\sim 1 \text{ keV}$, which we initially parameterize with a phenomenological blackbody of $kT = 0.18_{-0.01}^{+0.00} \text{ keV}$. There is also evidence for two distinct physical zones of low ($N_{\text{H}1} = 3.29_{-0.28}^{+0.18} \times 10^{21} \text{ cm}^{-2}$, $\log \xi_1 = 0.69_{-0.03}^{+0.07}$) to moderately ionized ($N_{\text{H}2} = 2.73_{-0.42}^{+0.51} \times 10^{21} \text{ cm}^{-2}$, $\log \xi_2 = 2.17_{-0.20}^{+0.21}$) intrinsic absorption. These components exist in addition to cold absorption by the Milky Way ($N_{\text{H}} = 1.71 \times 10^{20} \text{ cm}^{-2}$). We find that the power-law in this source has a spectral index of $\Gamma = 2.13 \pm 0.01$, which is slightly harder than the value determined for the time-averaged spectrum by Pounds et al. (2003) ($\Gamma = 2.21 \pm 0.01$). Unfortunately, these authors did not probe the spectrum below 3 keV, so we cannot compare our soft excess or warm absorption parameters to theirs.

The narrow Fe K α core of Mrk 766 has a rest-frame energy of $6.40 \pm 0.01 \text{ keV}$, consistent with neutral iron, and an $EW = 47 \pm 8 \text{ eV}$, consistent with the strength of the narrow line of neutral iron found by Pounds et al. Fitting this line with a Gaussian component leaves

significant residuals strongly indicative of the presence of a broad line. When this residual feature is fit with a broad Gaussian component its rest-frame energy is indicative of ionized iron: $E = 6.62 \pm 0.07 \text{ keV}$. Its width ($\sigma = 0.30 \pm 0.08 \text{ keV}$) is indicative of an origin $\sim 100 r_g$ from the black hole. This broad component is most successfully fit here with a `kdblur(reflion)` model (removing the now-unnecessary blackbody component), yielding comparable results to the disk reflection model employed to model the broad iron line in Pounds et al. (reduced $\chi^2 = 1.09$ in our work, compared with 1.11 in Pounds et al.), though with slightly tighter parameter constraints (e.g., $r_{\min} \leq 14 r_g$ in our work vs. $70 \pm 12 r_g$ in Pounds et al.). Our model also detects no absorption features above 8 keV, as discussed by Pounds et al., possibly due to our different approach toward modeling the reflection spectrum, i.e., the use of `reflion` vs. the `xion` model employed by Pounds et al. We note, however, that there is no significant difference between our `kdblur` and `rdblur` fits, or between our `diskline` and `laor` fits, indicating that we are not able to distinguish between a spinning and non-spinning black hole in this source using these data. The final best-fit results are shown in Table 4. Fig. 3 shows the iron line residual, best fit to this residual, and relative contributions of the individual model components, respectively. The `diskline` and `laor` fits are shown in Table 10, while comparisons of the ionized disk reflection spectrum with and without relativistic smearing can be found in Table 11.

4.2.4. 3C 273

3C 273 is the most distant source in our sample at a redshift of $z = 0.1583$. Classified as a bright variable quasar, this AGN displays a strong jet and during epochs of radio-loudness it possesses the flat X-ray spectrum of a blazar, with highly beamed jet emission (Türler et al. 2006). When the jet is reduced in strength, however, this source has been observed to exhibit Sy 1-type accretion disk signatures such as a broad iron line. A jet-minimum state occurred in March 1986 and allowed Robson et al. (1986) to identify a new near-infrared spectral component. An even better opportunity arose in early 2004, when the sub-millimeter flux of 3C 273 was observed to be almost two times lower than in 1986. This new minimum triggered a slew of simultaneous observations with instruments in all wavebands such as *INTEGRAL*, *XMM-Newton* and *RXTE*, among several other optical, radio and sub-millimeter telescopes. The 2 – 10 keV flux during this period was $F_{2-10} = 6.7 \times 10^{-11} \text{ erg cm}^{-2} \text{ s}^{-1}$. Such a low flux in 3C 273 has only been measured twice in the past, by *Ginga* in July 1987 (Turner et al. 1990) and by *BeppoSAX* on 18 July 1996 (Haardt et al. 1998), the latter of which was coincident with the low sub-mm flux mentioned above. This X-ray/sub-mm correlation strongly supports a synchrotron self-Compton origin for the X-ray jet emission in 3C 273.

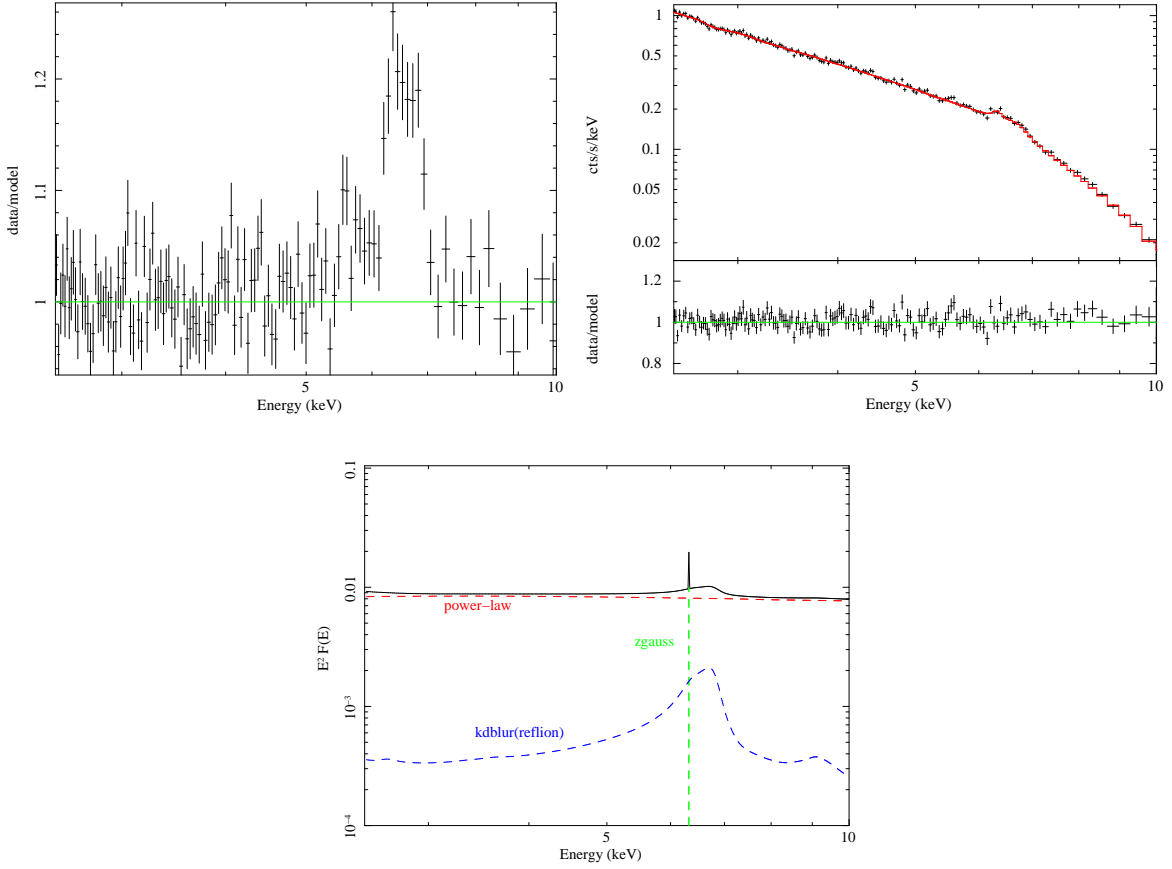


Fig. 3.— *Top left:* The 2.5–10.0 keV spectrum of Mrk 766 fit with a continuum composed of a power-law model modified by Galactic photoabsorption, a two-zone warm absorber model and a blackbody soft excess. $\chi^2/\nu = 1681/1315$ (1.28). *Top right:* The 2.5–10.0 keV best-fit model for Mrk 766, including our continuum model and an ionized disk reflection spectrum convolved with the `kdblur` relativistic smearing kernel. $\chi^2/\nu = 1426/1308$ (1.09). *Bottom:* An $E^2 F(E)$ plot depicting the relative flux in each of the model components in the spectrum.

Model Component	Parameter	Value
phabs	$N_{\text{H}} (\text{cm}^{-2})$	1.71×10^{20}
WA 1	$N_{\text{WA1}} (\text{cm}^{-2})$	$3.29^{+0.18}_{-0.28} \times 10^{21}$
	$\log \xi_{\text{WA1}}$	$0.69^{+0.07}_{-0.03}$
WA 2	$N_{\text{WA2}} (\text{cm}^{-2})$	$2.73^{+0.51}_{-0.42} \times 10^{21}$
	$\log \xi_{\text{WA2}}$	$2.17^{+0.21}_{-0.20}$
zpo	Γ_{po}	$2.13^{+0.01}_{-0.01}$
	flux ($\text{ph cm}^{-2} \text{s}^{-1}$)	$1.05^{+0.02}_{-0.04} \times 10^{-2}$
zgauss	E (keV)	$6.40^{+0.01}_{-0.01}$
	flux ($\text{ph cm}^{-2} \text{s}^{-1}$)	$3.80^{+1.94}_{-2.03} \times 10^{-6}$
	EW (eV)	47^{+8}_{-8}
kdblur	α	$2.29^{+1.35}_{-0.45}$
	i ($^{\circ}$)	28^{+4}_{-5}
	$r_{\text{min}} (r_{\text{g}})$	14^{+0}_{-14}
	$r_{\text{max}} (r_{\text{g}})$	400
reflion	Fe/solar	1.0
	$\xi_{\text{refl}} (\text{erg cm}^{-1} \text{s}^{-1})$	961^{+329}_{-465}
	Γ_{refl}	$2.13^{+0.01}_{-0.01}$
	R_{refl}	$0.01^{+0.17}_{-0.01}$
	flux ($\text{ph cm}^{-2} \text{s}^{-1}$)	$1.38^{+8.25}_{-0.64} \times 10^{-7}$
χ^2/ν		1426/1308 (1.09)

Table 4: Best-fitting model parameters for the 2.5 – 10.0 keV spectrum of Mrk 766, including components and parameter values from 0.6 – 1.5 keV for completeness. The energies from 1.5 – 2.5 keV were not included due to the presence of absorption edges from the *XMM-Newton* mirrors. Error bars are quoted at 90% confidence. We required the **zgauss** line representing the core of the Fe $K\alpha$ feature to be intrinsically narrow, i.e., $\sigma = 0$ keV. Redshifts were frozen at the cosmological value for the source, in this case $z = 0.0130$. A two-zone warm absorber is present in this object, as in MCG–6–30–15 and many other Sy 1 sources. We were not able to constrain the iron abundance for the ionized disk model, so we elected to fix it at the solar value.

Türler et al. obtained a 20 ks *XMM-Newton* observation of 3C 273 during this jet-minimum state in June 2004. We use their (reprocessed) thin-filter EPIC-pn observation in the interest of collecting as many photons as possible, though due to photon pile-up it is necessary to exclude the centralmost region of the source, as detailed by the authors (Türler et al. 2006). In our filtered data set we capture $\sim 3.2 \times 10^5$ photons.

Türler et al. note the inadequacy of a simple photoabsorbed power-law fit to the data. Their best fit to the continuum is achieved using two power-law components: $\Gamma_{\text{hard}} = 1.63 \pm 0.02$ and $\Gamma_{\text{soft}} = 2.69 \pm 0.06$, with the hard component flux ~ 2.3 times the soft flux. Both components were modified by Galactic photoabsorption with $N_{\text{H}} = 1.79 \times 10^{20} \text{ cm}^{-2}$. We based our initial continuum fit on theirs, with two power-law components: $\Gamma_{\text{hard}} = 1.72_{-0.28}^{+0.11}$ and $\Gamma_{\text{soft}} = 3.01_{-0.71}^{+1.29}$, both consistent with the Türler et al. results. The ratio we calculate between the fluxes of the hard and soft power-law components is ~ 4.18 , however. This is significantly higher than that calculated by Türler et al., and the error bars on the spectral indices, in particular, led us to consider eliminating the soft component. We did so, but still found it necessary to parameterize the remaining soft excess with a thermal `bbbody` model at first ($kT = 0.14_{-0.02}^{+0.03} \text{ keV}$). Such a component is not entirely phenomenological in nature, however: in many radio-loud sources a soft thermal excess has been noted, and is often interpreted as arising from the interaction of the jet with the surrounding ISM (e.g., Brenneman et al. 2009). Our best-fitting continuum model, therefore, has a blackbody and only one power-law component at $\Gamma = 1.84_{-0.10}^{+0.46}$ and exhibits the same statistical goodness-of-fit as the two power-law model.

Evidence for excess emission from 2.5 – 7.0 keV was also found by Türler et al., supporting the presence of a broad Fe K α line when 3C 273 is in a jet-minimum state. The authors quote this excess as significant at the 6σ level with an integrated flux of $2.6 \pm 0.4 \times 10^{-4} \text{ ph cm}^{-2} \text{ s}^{-1}$, corresponding to an $EW = 166 \pm 26 \text{ eV}$. These values are consistent with those reported from previous observations of the source in a jet-minimum state (Kataoka et al. 2002; Page et al. 2004; Yaqoob & Serlemitsos 2000). The breadth of the excess is not satisfactorily fitted by a Gaussian line or a `diskline` component from a non-rotating BH. If the line extent is real, the only remaining explanation, according to the authors, is that it is emitted from around a near-extreme Kerr BH. The sharp edge of the iron line at 7 keV suggests that the angle of inclination of the accretion disk is $35 - 40^\circ$ (Türler et al. 2006). This is contrary to radio observations of the source which have measured superluminal velocity in the jet consistent with it having an inclination angle of $\leq 14^\circ$ to the line of sight (Ballantyne et al. 2004). Such a marked difference between the disk and jet inclination angles may imply a warped disk, or perhaps it may mean that the jet inclination is different on smaller, unresolvable scales. Deeper observations are needed in order to resolve this discrepancy.

We find evidence for a similar excess around the Fe K region in our analysis. Interestingly, we do *not* see a narrow emission line at 6.4 keV, but rather the narrow line core seems to coincide with the He-like line of Fe K α at 6.68 ± 0.07 keV with an $EW = 49_{-35}^{+37}$ eV. This may mean that the gas in this system is significantly ionized, which would not be surprising in such an active source. Indeed, this hypothesis is lent credence by fitting a full `reflion` disk spectrum to the data (which also renders the soft blackbody component obsolete): the disk ionization parameter is only constrained to $\xi < 5689$ erg cm s $^{-1}$. Visually, the residuals left over after fitting this narrow line suggest the presence of a broad component. Modeling this component with our analysis method provides, at best, only a marginal improvement in the global goodness-of-fit ($\Delta\chi^2/\Delta\nu = -9/-6$), perhaps due to the distance of the source and the paucity of photons in the data as compared with the other sources in our sample. With a 20 ks observation we have collected $\sim 3 \times 10^5$ photons from 2.5 – 10 keV. Given more observing time and a larger number of (pile-up free) photons, our line analysis would be significantly improved. Taking into account these caveats about the robustness of the broad line, the `kdblur(reflion)` model still provides the best fit, as shown in Table 5, though this fit is statistically no better than that of a broad Gaussian or `laor` line. The disk emission is highly centrally concentrated with $\alpha = 6.04_{-2.06}^{+3.94}$, consistent with the small inner radius of emission fit by the model: $r_{\min} \leq 3.73 r_g$. The X-ray constraints on the inclination angle of the disk are consistent with those obtained by Türler et al., within errors: $i = 58_{-22}^{+15}$ degrees. The amount of reflection in this source is difficult to constrain without better photon statistics: $R_{\text{refl}} = 0.89_{-0.89}^{+6311}$. Fig. 4 shows the iron line residual, best fit to this residual, and relative contributions of the individual model components in the best fit, respectively. The `diskline` and `laor` fits are shown in Table 10, while comparisons of the ionized disk reflection spectrum with and without relativistic smearing can be found in Table 11.

4.2.5. NGC 2992

NGC 2992 is a Sy 1.9 galaxy ($z = 0.0077$) that appears to show a broad iron line even though it is highly obscured. This source has been the subject of intense study due to the variability of its X-ray emission (Gilli et al. 2000). In 1997 and 1998, *BeppoSAX* caught NGC 2992 transitioning from a Compton-thick to a Compton-thin state, resulting in an order of magnitude increase in its X-ray luminosity as well as a qualitative difference in its spectral appearance, with more disk features (e.g., broad lines) being seen in several wavelengths. In the two *BeppoSAX* pointings, NGC 2992 displays 2 – 10 keV X-ray fluxes of 0.63 and 7.4×10^{-11} erg cm $^{-2}$ s $^{-1}$, respectively (Gilli et al. 2000).

We use the May 2003 *XMM-Newton* observation of NGC 2992, totaling 29 ks, which

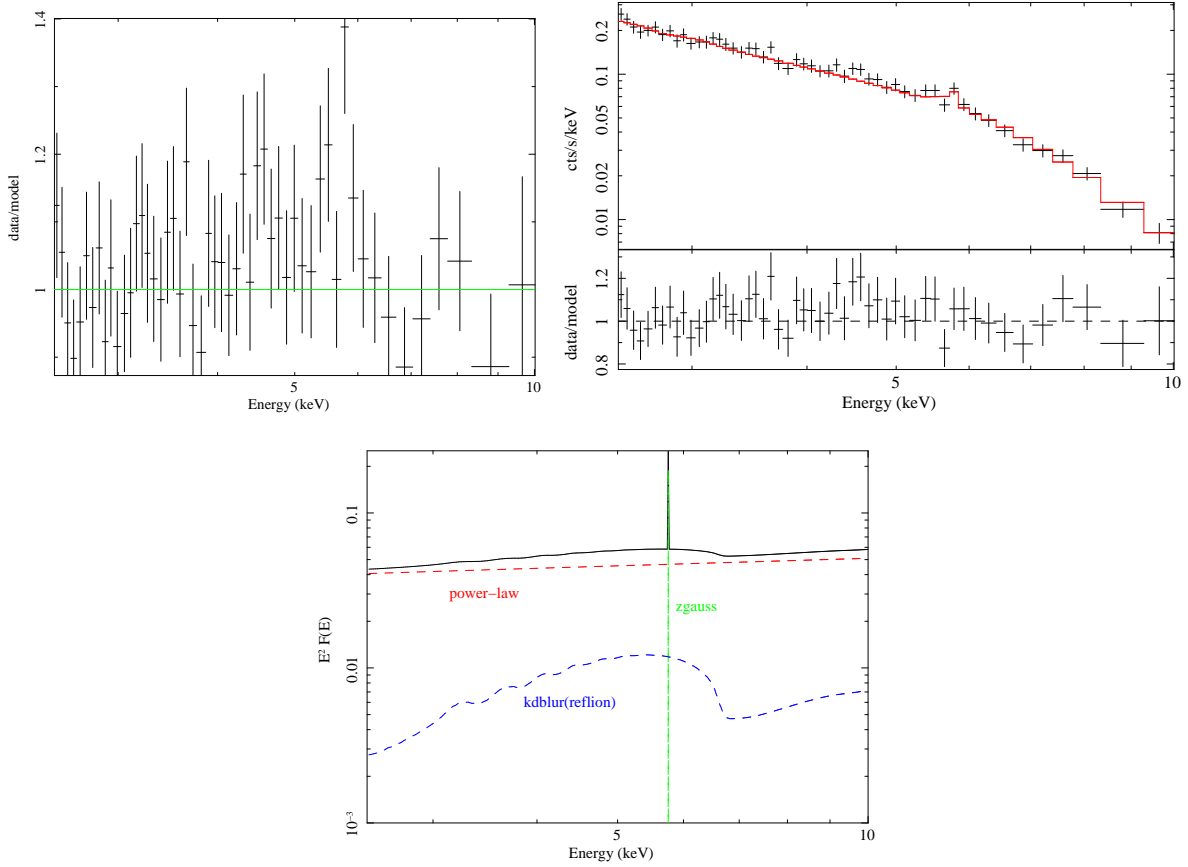


Fig. 4.— *Top left:* The 2.5 – 10.0 keV spectrum of 3C 273 fit with a power-law + black-body model modified by Galactic photoabsorption. $\chi^2/\nu = 248/270$ (0.92). *Top right:* The 2.5 – 10.0 keV best-fit model for 3C 273, including our continuum model and an ionized disk reflection spectrum convolved with the kdblur relativistic smearing kernel. $\chi^2/\nu = 229/264$ (0.86). *Bottom:* An $E^2 F(E)$ plot depicting the relative flux in each of the model components in the spectrum.

Model Component	Parameter	Value
phabs	$N_{\text{H}} (\text{cm}^{-2})$	1.79×10^{20}
zpo	Γ_{po}	$1.84^{+0.46}_{-0.10}$
	flux ($\text{ph cm}^{-2} \text{s}^{-1}$)	$4.61^{+0.35}_{-0.59} \times 10^{-2}$
zgauss	E (keV)	$6.68^{+0.07}_{-0.07}$
	flux ($\text{ph cm}^{-2} \text{s}^{-1}$)	$1.00^{+0.75}_{-0.72} \times 10^{-4}$
	EW (eV)	49^{+37}_{-35}
kdblur	α	$6.04^{+3.94}_{-2.06}$
	i ($^{\circ}$)	58^{+15}_{-22}
	$r_{\text{min}} (r_{\text{g}})$	$3.73^{+0.00}_{-3.73}$
	$r_{\text{max}} (r_{\text{g}})$	400
refl	Fe/solar	1.0
	$\xi_{\text{refl}} (\text{erg cm}^{-1} \text{s}^{-1})$	82^{+5607}_{-82}
	Γ_{refl}	$1.84^{+0.46}_{-0.10}$
	R_{refl}	$0.89^{+6311}_{-0.89}$
	flux ($\text{ph cm}^{-2} \text{s}^{-1}$)	$4.78^{+10755}_{-3.65} \times 10^{-5}$
χ^2/ν		229/264 (0.86)

Table 5: Best-fitting model parameters for the 2.5 – 10.0 keV spectrum of 3C 273, including components and parameter values from 0.6–1.5 keV for completeness. As before, the energies from 1.5 – 2.5 keV were not included due to the presence of absorption edges from the *XMM-Newton* mirrors. Error bars are quoted at 90% confidence. We required the **zgauss** line representing the core of the Fe $K\alpha$ feature to be intrinsically narrow, i.e., $\sigma = 0$ keV. Interestingly, this line was found at a moderate ionization state of iron (6.68 keV) rather than at the neutral rest-frame energy of 6.4 keV. Redshifts were frozen at the cosmological value for the source, in this case $z = 0.1583$. No warm absorption is seen in this object. Note the large error bars on the value of R_{refl} that we calculate. These are likely an artifact of the relatively low photon count for this observation.

translates to $\sim 3.4 \times 10^5$ photons in the filtered data set. This observation appears to be unpublished, so all the fit values referenced herein are our own, compiled using the reduction and analysis methods detailed in §3.

Upon first inspection, it is immediately clear that NGC 2992 is heavily absorbed below ~ 2 keV. Though statistical evidence exists for a soft excess, none of the telltale signatures of intrinsic warm absorption are present, and the flux decreases precipitously at soft energies. When a simple photoabsorbed power-law model is applied to the continuum, the remaining residuals on the soft end indicate that some absorption remains unaccounted for. Including a `zpcfabs` component to model this intrinsic absorption with a partial-coverer in addition to the Galactic hydrogen column of $N_{\text{H}} = 5.26 \times 10^{20} \text{ cm}^{-2}$ neatly corrects the discrepancy. The final continuum parameters are $N_{\text{H}2} = 5.39_{-0.08}^{+0.13} \times 10^{21} \text{ cm}^{-2}$ with a covering fraction of $f_{\text{cov}} = 95_{-0}^{+1}\%$ absorbing a power-law of photon index of $\Gamma = 1.71_{-0.04}^{+0.06}$.

The Fe $K\alpha$ line is present with a narrow core at $6.43_{-0.02}^{+0.01}$ keV and $EW = 36_{-9}^{+12}$ eV. Significant residuals remain surrounding the core, however, suggestive of the presence of a broad component to the Fe $K\alpha$ line. Adding a broad Gaussian component at 6.40 keV results in a significant improvement in the global goodness-of-fit of $\Delta\chi^2/\Delta\nu = -25/-3$, and the fitted width of $\sigma = 0.20 - 0.51$ keV implies an origin of $\sim 30 - 190 r_{\text{g}}$ from the black hole assuming a Keplerian accretion disk. The fit is only marginally improved by modeling this broad component with a `diskline`, `laor` or relativistically smeared ionized disk reflection model, though the best statistical fit is technically achieved with a `kdblur(reflion)` model. Nonetheless, due to a lack of significant difference between the `rdblur` and `kdblur` fits, we cannot distinguish between a spinning and non-spinning black hole in this source, nor can we definitively affirm the presence of relativistic effects on the Fe $K\alpha$ line profile. See Table 6 for model parameters and error bars. Fig. 5 shows the iron line residual, best fit to this residual, and relative contributions of the individual model components for the best fit. The `diskline` and `laor` fits are shown in Table 10, while comparisons of the ionized disk reflection spectrum with and without relativistic smearing can be found in Table 11.

4.2.6. NGC 4051

NGC 4051, like NGC 2992, is a heavily absorbed Seyfert AGN (Sy 1.5; NLS1) seen to vary significantly in flux over the course of several observations (Guainazzi et al. 1996; Lamer et al. 2003). The source is at a redshift of $z = 0.0023$ and has a typical flux on the order of a few times $10^{-11} \text{ erg cm}^{-2} \text{ s}^{-1}$, though as stated above, this flux can vary significantly on a variety of time scales, along with the spectral characteristics of the source. Unusually low flux states in this object can last for weeks to months, during which time the

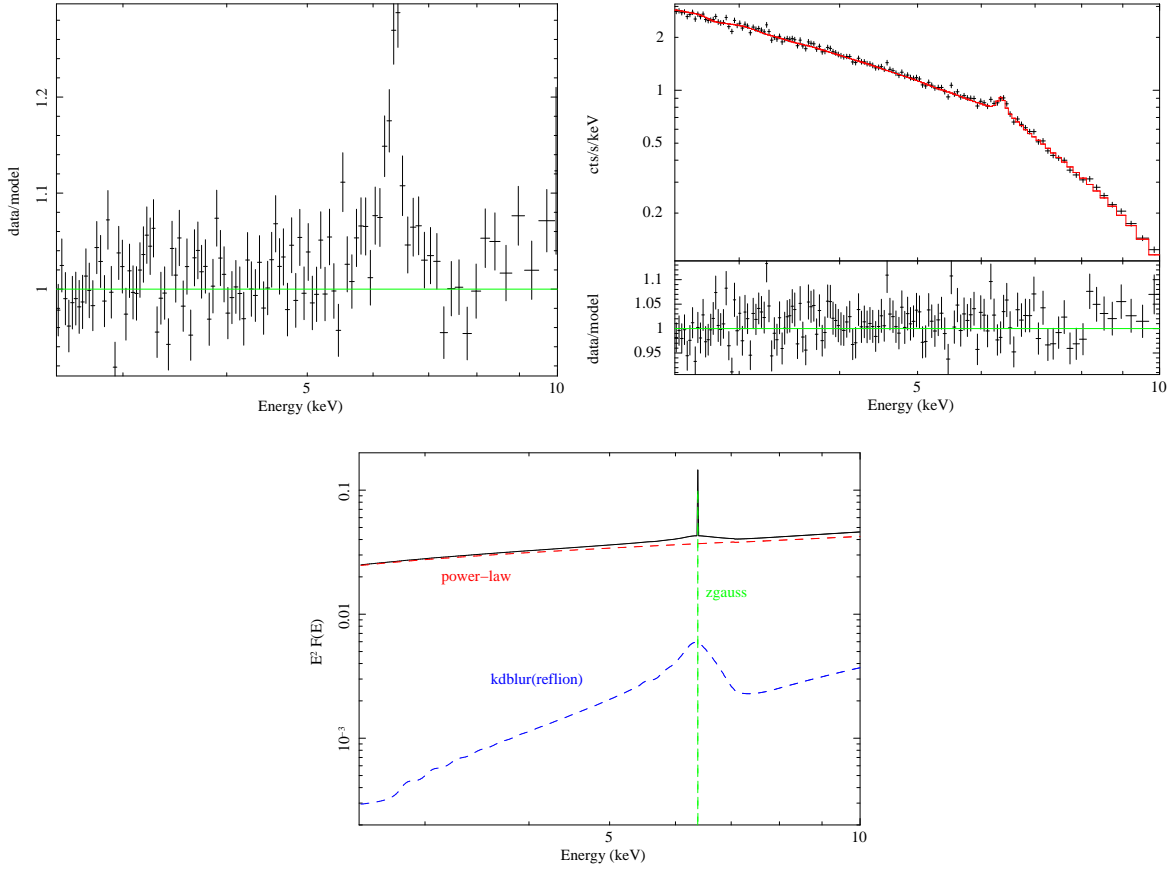


Fig. 5.— *Top left*: The 2.5–10.0 keV spectrum of NGC 2992 fit with a continuum composed of a power-law model modified by Galactic photoabsorption as well as intrinsic absorption by neutral hydrogen. $\chi^2/\nu = 1581/1317$ (1.20). *Top right*: The 2.5–10.0 keV best-fit model for NGC 2992, including our continuum model and an ionized disk reflection spectrum convolved with the `kdblur` relativistic smearing kernel. $\chi^2/\nu = 1396/1310$ (1.07). *Bottom*: An $E^2 F(E)$ plot depicting the relative flux in each of the model components in the spectrum.

Model Component	Parameter	Value
phabs	N_{H} (cm^{-2})	5.26×10^{20}
zpcfabs	N_{H2} (cm^{-2})	$5.39_{-0.08}^{+0.13} \times 10^{21}$
	F_{cov} (%)	95_{-0}^{+1}
zpo	Γ_{po}	$1.71_{-0.04}^{+0.06}$
	flux ($\text{ph cm}^{-2} \text{s}^{-1}$)	$2.20_{-0.06}^{+0.13} \times 10^{-2}$
zgauss	E (keV)	$6.43_{-0.02}^{+0.01}$
	flux ($\text{ph cm}^{-2} \text{s}^{-1}$)	$3.84_{-0.98}^{+1.24} \times 10^{-5}$
	EW (eV)	36_{-9}^{+12}
kdblur	α	$3.00_{-3.00}^{+7.00}$
	i ($^{\circ}$)	43_{-10}^{+4}
	r_{min} (r_{g})	$3.64_{-0.73}^{+1.29}$
	r_{max} (r_{g})	400
reflion	Fe/solar	1.0
	ξ_{refl} ($\text{erg cm}^{-1} \text{s}^{-1}$)	30_{-0}^{+37}
	Γ_{refl}	$1.71_{-0.04}^{+0.06}$
	R_{refl}	$0.49_{-0.37}^{+0.10}$
	flux ($\text{ph cm}^{-2} \text{s}^{-1}$)	$1.82_{-0.73}^{+0.34} \times 10^{-5}$
χ^2/ν		1396/1310 (1.07)

Table 6: Best-fitting model parameters for the 2.5–10.0 keV spectrum of NGC 2992, including components and parameter values from 0.6 – 1.5 keV for completeness. The energies from 1.5 – 2.5 keV were not included due to the presence of absorption edges from the *XMM-Newton* mirrors. Error bars are quoted at 90% confidence. Redshifts were frozen at the cosmological value for the source, in this case $z = 0.0077$. No evidence for warm absorption is detected. The iron abundance of the ionized disk could not be constrained, so it was held fixed at the solar value.

X-ray spectrum shows a hard continuum power-law of spectral slope $\Gamma \sim 1$, but is dominated by a softer component at lower energies with $\Gamma \sim 3$ (Uttley et al. 2004). A highly broadened and redshifted iron line has also been noted in the low flux state of NGC 4051 with *RXTE*, suggesting that reflection features from the accretion disk close to the BH may remain constant in this source in spite of the large variations in continuum properties (Uttley et al. 2003).

NGC 4051 was observed with *XMM-Newton* in May 2001 for a duration of 117 ks, yielding $\sim 2.5 \times 10^6$ photons in the filtered data set. The EPIC-pn results were first reported by Mason et al., and suggested a continuum described by a power-law “pivoting” around 100 keV, according to a simultaneous observation with *RXTE*. Ultraviolet emission from the Optical Monitor on *XMM-Newton* was found to lag the X-ray emission by ~ 0.2 days, indicating that it is likely reprocessed X-ray emission. The X-ray emission itself showed variability on time scales as small as 1 – 2 hours (Mason et al. 2002). These results were expanded upon by Pounds et al., who noted the intermediate flux of the source at this time and validated the presence of both an iron line and a thermal soft excess during the May 2001 observation (Pounds et al. 2004). Ponti et al. recently re-analyzed this observation as well as a lower-flux pointing from November 2002 and reinforced the veracity of this model, while also considering the comparable efficacy of a model dominated by ionized reflection from radii quite close to the BH (Ponti et al. 2006).

We have also focused on the May 2001 observation of NGC 4051, following the reduction and analysis of Mason et al. and Ponti et al. but using modern calibration files. Because we do not employ high energy data above 10 keV in our analysis, we find that the underlying 0.6 – 10 keV continuum is well fit by a single power-law component with photon index $\Gamma = 2.36_{-0.20}^{+0.36}$. This power-law is modified by Galactic photoabsorption from neutral hydrogen with $N_{\text{H}} = 1.32 \times 10^{20} \text{ cm}^{-2}$ as well as ionized intrinsic absorption with $N_{\text{H}} = 2.77_{-0.51}^{+3.08} \times 10^{22} \text{ cm}^{-2}$ and $\xi = 81_{-2}^{+1} \text{ erg cm s}^{-1}$. A soft excess is seen below ~ 1 keV, as in so many other Seyfert galaxies. The best fit to this feature is initially achieved with a thermal blackbody component, with $kT = 0.10 \pm 0.01$.

A narrow $6.40_{-0.03}^{+0.01}$ keV Gaussian was successfully fit to the core of the Fe $K\alpha$ line in this source, though we note significant residuals marking the red and blue wings of a broadened line. The narrow core has an equivalent width of $EW = 59_{-11}^{+14}$ eV. The remaining broad line is best fit here with either a `diskline` or a `laor` model with $EW \sim 35$ eV, but in each case fitting this single relativistic disk line leaves several parameters poorly constrained. A better fit to the entire spectrum is achieved by convolving a static ionized disk reflection spectrum model (`reflion`) with a relativistic smearing kernel. This more physical model also has the advantage of self-consistently accounting for the observed soft excess without the need to

include a phenomenological blackbody component. The spectrum of NGC 4051 is equally well fit by a `kdblur(reflion)` or an `rdblur(reflion)` model, though the `kdblur` model is cited as the best fit due to slightly tighter parameter constraints on the inner radius of disk emission ($r_{\min} = 6.94_{-2.95}^{+2.41} r_g$). Full parameter values and 90% confidence error bars are listed in Table 7. Fig. 6 shows the iron line residual, best fit to this residual, and relative contributions of the individual model components, respectively. The `diskline` and `laor` fits are shown in Table 10, while comparisons of the ionized disk reflection spectrum with and without relativistic smearing can be found in Table 11.

4.2.7. Ark 120

Ark 120 is a bright Sy 1 AGN at a redshift of $z = 0.0327$, and has a relatively constant 2–10 keV X-ray flux of $F_{2-10} \sim 2.50 \times 10^{-11} \text{ erg cm}^{-2} \text{ s}^{-1}$ (Vaughan et al. 2004). The source is radio-quiet, and due to a lack of observed evidence for intrinsic absorption, Ark 120 has been labeled a “bare” Sy 1 nucleus (Ward et al. 1987; Vaughan et al. 2004). Ark 120 has been observed by most of the major X-ray observatories. An *EXOSAT* observation showed the source to have a steep soft X-ray spectrum (Turner & Pounds 1989), as did a subsequent *ROSAT* observation (Brandt et al. 1993). Furthermore, as mentioned above, these X-ray observations showed no indication of any warm absorption features. Similar findings were seen in ultraviolet observations (Crenshaw et al. 1999; Crenshaw & Kraemer 2001).

The source was observed by *XMM-Newton* in August 2003 for an effective duration of 100 ks ($\sim 2.3 \times 10^6$ photons by Vaughan et al. (2004)). We follow the data reduction and analysis of these authors, using the latest calibration files, though we restrict our attention to the EPIC-pn camera data. Vaughan et al. find that the continuum emission is well described by a simple photoabsorbed power-law model with no evidence for complex absorption intrinsic to the system. This finding is substantiated by a comparison to the spectrum of 3C 273 in its radio-loud state, when the source is dominated by jet emission and displays a very flat, featureless X-ray spectrum lacking intrinsic emission and absorption features. Vaughan et al. calculated the ratio between the spectra of Ark 120 and 3C 273, then normalized it by a spectral model for 3C 273. The resulting spectrum clearly shows that Ark 120, too, possesses a flat, featureless continuum above ~ 1 keV and that its only significant emission line is that of Fe $K\alpha$ at 6.4 keV. The authors use a multiple blackbody component (among many other models, with varying degrees of success) for the soft excess to reduce residuals left over from the power-law fit below ~ 1 keV, and a slight curvature of the continuum is noted at higher energies that is thought to indicate the presence of disk reflection in this source (Vaughan et al. 2004).

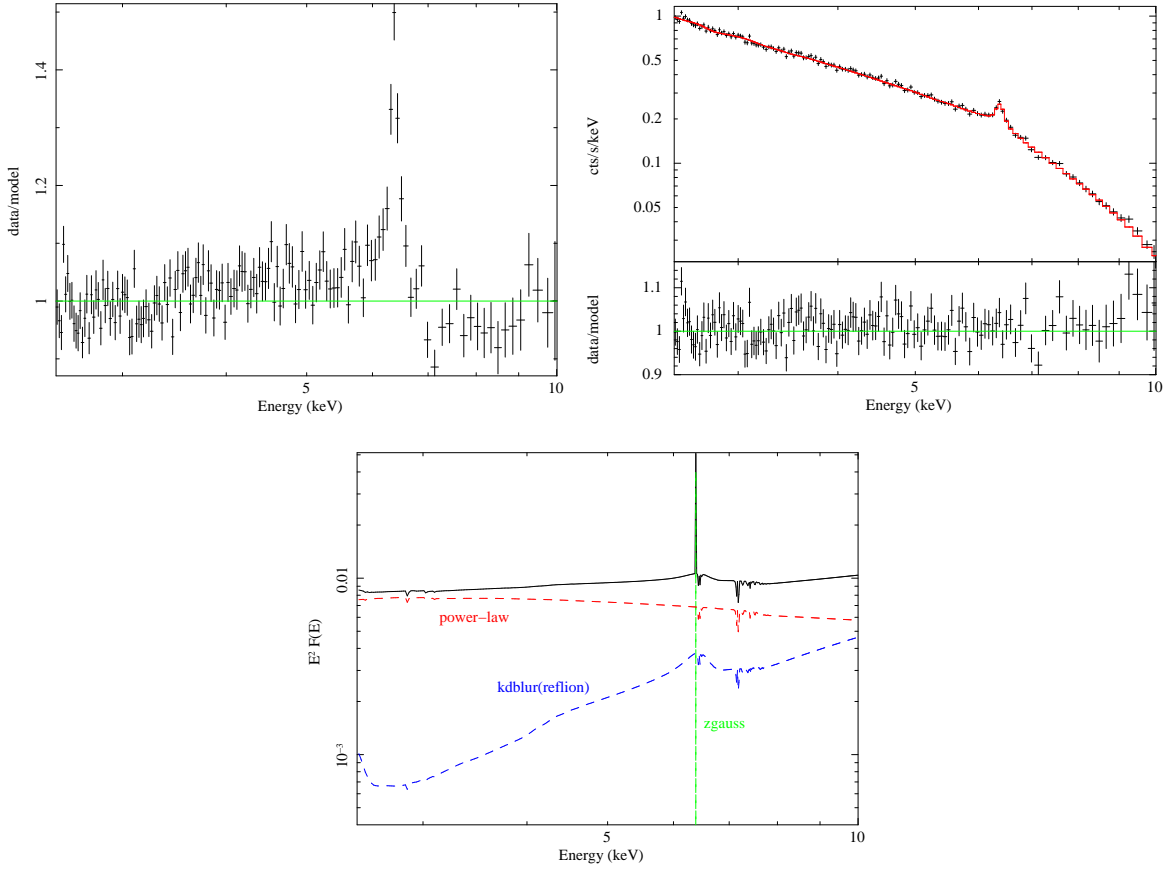


Fig. 6.— *Top left:* The 2.5 – 10.0 keV spectrum of NGC 4051 fit with a continuum composed of a power-law model modified by Galactic photoabsorption, a warm absorber model and a blackbody soft excess. $\chi^2/\nu = 1837/1402$ (1.31). *Top right:* The 2.5 – 10.0 keV best-fit model for NGC 4051, including our continuum model, a narrow Fe $K\alpha$ line core and an ionized disk reflection spectrum convolved with the `kdblur` relativistic smearing kernel. $\chi^2/\nu = 1468/1392$ (1.05). *Bottom:* An $E^2 F(E)$ plot depicting the relative flux in each of the model components in the spectrum.

Model Component	Parameter	Value
phabs	N_{H} (cm^{-2})	1.32×10^{20}
WA	N_{WA} (cm^{-2})	$2.77^{+3.08}_{-0.51} \times 10^{22}$
	$\log \xi_{\text{WA}}$	$1.91^{+0.17}_{-0.27}$
zpo	Γ_{po}	$2.36^{+0.36}_{-0.20}$
	flux ($\text{ph cm}^{-2} \text{s}^{-1}$)	$1.39^{+0.09}_{-0.28} \times 10^{-2}$
zgauss	E (keV)	$6.40^{+0.01}_{-0.03}$
	flux ($\text{ph cm}^{-2} \text{s}^{-1}$)	$1.53^{+0.37}_{-0.29} \times 10^{-5}$
	EW (eV)	59^{+14}_{-11}
kdblur	α	$8.29^{+1.71}_{-8.29}$
	i ($^{\circ}$)	33^{+6}_{-9}
	r_{min} (r_{g})	$6.94^{+2.41}_{-2.95}$
	r_{max} (r_{g})	400
reflion	Fe/solar	$0.42^{+0.20}_{-0.08}$
	ξ_{refl} ($\text{erg cm}^{-1} \text{s}^{-1}$)	99^{+26}_{-61}
	Γ_{refl}	$2.36^{+0.36}_{-0.20}$
	R_{refl}	$0.88^{+12.94}_{-0.43}$
	flux ($\text{ph cm}^{-2} \text{s}^{-1}$)	$2.77^{+10.66}_{-0.88} \times 10^{-5}$
χ^2/ν		1468/1392 (1.05)

Table 7: Best-fitting model parameters for the 2.5–10.0 keV spectrum of NGC 4051, including components and parameter values from 0.6 – 1.5 keV for completeness. The energies from 1.5 – 2.5 keV were not included due to the presence of absorption edges from the *XMM-Newton* mirrors. Error bars are quoted at 90% confidence. We required the 6.4 keV **zgauss** line to be intrinsically narrow, i.e., $\sigma = 0$ keV. Redshifts were frozen at the cosmological value for the source, in this case $z = 0.0023$. A warm absorber is present in this object, as in many other Sy 1 sources.

Our continuum fit is consistent with that of Vaughan et al. , though we find a statistical need for only two blackbody components to parameterize the soft excess emission, rather than three: $kT_1 = 0.19 \pm 0.01$ keV and $kT_2 = 0.08_{-0.00}^{+0.01}$ keV. These two temperatures are within errors of the first two blackbodies of Vaughan et al. , but we do not detect the third component at $kT \sim 0.67$ keV robustly. The hard X-ray continuum is well represented by a power-law of $\Gamma = 2.11_{-0.07}^{+0.03}$, again consistent with the Vaughan et al. value within errors. The value of the Galactic absorbing column is taken as $N_{\text{H}} = 1.26 \times 10^{21} \text{ cm}^{-2}$.

Vaughan et al. detected the presence of broad and narrow components to the 6.4 keV Fe K α line ($EW_{\text{broad}} \sim 100$ eV, $EW_{\text{narrow}} \sim 40$ eV). The narrow component could easily be fit with a 6.4 keV Gaussian profile, as was our Fe K α narrow core, but Vaughan et al. found that a `diskline` model worked best for their broad component ($r_{\text{min}} \approx 144 r_{\text{g}}$). Interestingly, this broad component fit to a rest-frame energy of 6.56 keV rather than 6.4 keV, with the latter yielding a substantially worse global fit ($\Delta\chi^2 = +21.5$) (Vaughan et al. 2004). This energy corresponds to the line emission being dominated by intermediately ionized iron (Fe XX-XXII), meaning that resonant trapping and the Auger effect should destroy the line (Ross et al. 1996).

In an effort to solve this puzzle we have fit our iron line profile with three narrow Gaussian components, the first two at 6.40 ± 0.01 keV and $7.00_{-0.03}^{+0.02}$ keV, representing neutral iron and a likely blend of highly ionized H-like Fe K α and Fe K β , respectively. The lines have $EW_{\text{cold}} = 36_{-8}^{+17}$ eV and $EW_{\text{ion}} = 28_{-8}^{+7}$ eV. After an initial attempt to fit the broad residual remaining, there is evidence for a third narrow line as well at $6.75_{-0.07}^{+0.04}$ keV ($EW = 14_{-4}^{+8}$ eV), indicating the presence of moderately ionized iron. The addition of this component improves the fit by $\Delta\chi^2 = -19$ for two additional degrees of freedom. This fit leaves a residual broad feature nicely centered at 6.4 keV, which renders this scenario physically consistent with other systems and removes the need to explain the presence of the broad line of iron in an intermediate state of ionization. We then achieve a best fit to the broad component using a Schwarzschild `rdblur(reflion)` model, which also nicely accounts for the additional curvature noted in the spectrum at higher energies by Vaughan et al. , as well as the soft excess we had initially modeled with phenomenological blackbody components. The best-fit parameter values and error bars are presented in Table 8. Fig. 7 shows the iron line residual, best fit to this residual, and relative contributions of the individual model components for the best fit. The `diskline` and `laor` fits are shown in Table 10, while comparisons of the ionized disk reflection spectrum with and without relativistic smearing can be found in Table 11.

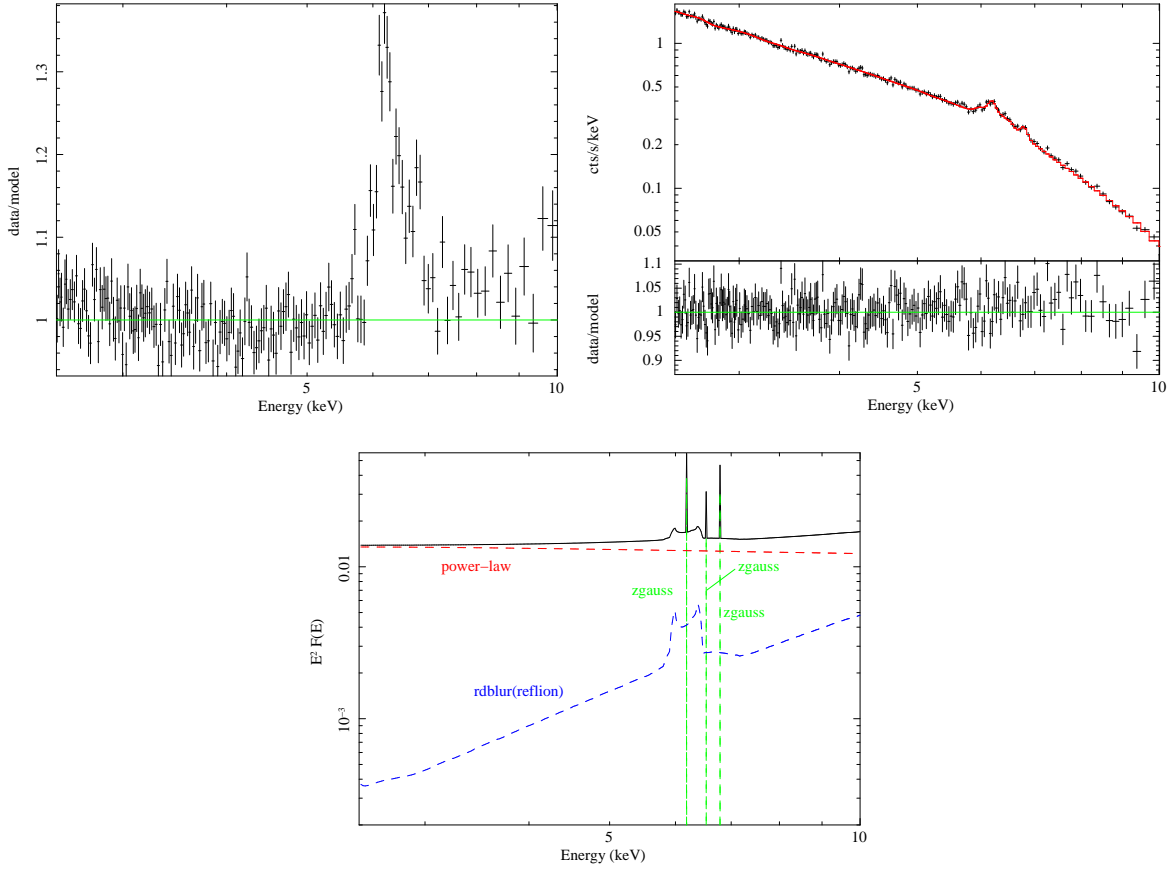


Fig. 7.— *Top left:* The 2.5 – 10.0 keV spectrum of Ark 120 fit with a continuum composed of a power-law model modified by Galactic photoabsorption and a two-zone blackbody soft excess. $\chi^2/\nu = 2153/1428$ (1.51). *Top right:* The 2.5 – 10.0 keV best-fit model for Ark 120, including our continuum model and an ionized disk reflection spectrum convolved with the **rdblur** relativistic smearing kernel. $\chi^2/\nu = 1511/1418$ (1.07). *Bottom:* An $E^2 F(E)$ plot depicting the relative flux in each of the model components in the spectrum.

Model Component	Parameter	Value
phabs	$N_{\text{H}} (\text{cm}^{-2})$	1.26×10^{21}
zpo	Γ_{po}	$2.11^{+0.03}_{-0.07}$
	flux (ph cm $^{-2}$ s $^{-1}$)	$1.64^{+0.05}_{-0.12} \times 10^{-2}$
zgauss	E (keV)	$6.40^{+0.01}_{-0.01}$
	flux (ph cm $^{-2}$ s $^{-1}$)	$1.65^{+0.32}_{-0.35} \times 10^{-5}$
	EW (eV)	36^{+17}_{-8}
zgauss	E (keV)	$6.75^{+0.04}_{-0.07}$
	flux (ph cm $^{-2}$ s $^{-1}$)	$5.73^{+3.08}_{-1.82} \times 10^{-6}$
	EW (eV)	14^{+8}_{-4}
zgauss	E (keV)	$7.00^{+0.02}_{-0.03}$
	flux (ph cm $^{-2}$ s $^{-1}$)	$1.01^{+0.26}_{-0.29} \times 10^{-5}$
	EW (eV)	28^{+7}_{-8}
rdblur	α	$1.31^{+0.61}_{-1.31}$
	i ($^{\circ}$)	41^{+15}_{-6}
	$r_{\text{min}} (r_{\text{g}})$	6^{+74}_{-6}
	$r_{\text{max}} (r_{\text{g}})$	400
reflion	Fe/solar	0.50
	$\xi_{\text{refl}} (\text{erg cm}^{-1} \text{s}^{-1})$	30^{+5}_{-30}
	Γ_{refl}	$2.11^{+0.03}_{-0.07}$
	R_{refl}	$1.75^{+0.67}_{-0.95}$
	flux (ph cm $^{-2}$ s $^{-1}$)	$2.09^{+0.80}_{-1.37} \times 10^{-5}$
χ^2/ν		1511/1418 (1.07)

Table 8: Best-fitting model parameters for the 2.5 – 10.0 keV spectrum of Ark 120, including components and parameter values from 0.6 – 1.5 keV for completeness. The energies from 1.5 – 2.5 keV were not included due to the presence of absorption edges from the *XMM-Newton* mirrors. Error bars are quoted at 90% confidence. We required the **zgauss** lines to be intrinsically narrow, i.e., $\sigma = 0$ keV. Redshifts were frozen at the cosmological value for the source, in this case $z = 0.0327$.

4.2.8. Fairall 9

Fairall 9 is a radio-quiet Sy 1 galaxy with an elliptical companion, both at a moderate redshift of $z = 0.047$. This source has not been observed to undergo very large changes in X-ray flux over the time it has been observed: the typical 2 – 10 keV flux of Fairall 9 is $F_{2-10} \sim 1.5 - 5.0 \times 10^{-11} \text{ erg cm}^{-2} \text{ s}^{-1}$ (Reynolds 1997; Gondoin et al. 2001). Previous X-ray observations with *ASCA* show that the source has a continuum well-described by a photoabsorbed power-law with a fluorescent Fe $K\alpha$ line and a high-energy tail. The latter is a common signature of disk reflection, as has been discussed previously with respect to a number of other sources in this Section (Reynolds 1997; Nandra et al. 1997). A soft excess has also been detected below ~ 2 keV (Pounds et al. 1994), though no strong evidence of warm absorption has been observed in the soft spectrum (Gondoin et al. 2001).

The source was observed with *XMM-Newton* in July 2000 for an effective duration of ~ 29 ks (Jansen et al. 2001), resulting in a filtered EPIC-pn data set with $\sim 2.0 \times 10^5$ photons. The EPIC-pn data were presented in full by Gondoin et al. the following year (Gondoin et al. 2001). We have followed the general procedures for data reduction and analysis discussed by Gondoin et al., using the most up-to-date calibration files and software as we have for all other sources analyzed in this work.

Gondoin et al. find that continuum of Fairall 9 is best modeled with a photoabsorbed power-law ($\Gamma = 1.79_{-0.12}^{+0.15}$), in which the absorbing column density of neutral hydrogen gas is approximately equal to its Galactic value along the line of sight to this source ($N_{\text{H}} = 3.19 \times 10^{20} \text{ cm}^{-2}$). A soft excess is noted below ~ 2 keV, and an RGS analysis yielded a best-fitting blackbody model for this component: $kT = 0.17_{-0.07}^{+0.09}$ keV. Incorporating reflection from an ionized disk (`pexriv`) with solar abundances and a reflection fraction of $R_{\text{refl}} = 1.0$, the authors find that the high-energy tail is quite well modeled by a disk at an inclination angle of $i = 26^\circ$ (Gondoin et al. 2001). We have performed a slightly different fit to the EPIC-pn data only, replacing the `pexriv` component with a relativistically-blurred `relion` model, which also accounts naturally for the soft excess without employing a phenomenological blackbody component. The column density of neutral hydrogen absorption was again frozen at the Galactic value of $N_{\text{H}} = 3.19 \times 10^{20} \text{ cm}^{-2}$. We found that $\Gamma = 1.88_{-0.04}^{+0.20}$, and the disk inclination angle fit to $i \sim 54^\circ$, though its value could not be properly constrained. Unfortunately, due to the relatively small number of photons in the 0.5 – 10.0 keV spectrum, parameter constraints were more problematic for this source than for many of the others in our sample.

Gondoin et al. also note the presence of a ~ 6.4 keV Fe $K\alpha$ line in the spectrum with $EW \sim 120$ eV, which they modeled with a Gaussian component. Due to its relatively narrow profile, the line is suggested to originate from low-ionization material orbiting relatively far

out in the disk. Additionally, an Fe K absorption edge is also noted at 7.64 keV with $\tau = 0.18$, consistent with reflection from cold, optically thick material. We find that the inclusion of such an edge is not statistically robust in our model once reflection is included via `reflion` (which incorporates the iron edge), but we do find the narrow $6.40_{-0.02}^{+0.01}$ keV line in emission and model it with a narrow Gaussian feature representing the core of the Fe K α line. This feature has an $EW = 115_{-20}^{+20}$ eV, but even after its inclusion residual features remain indicating the presence of other unmodeled narrow lines as well as a potential broader iron line component as evidenced by a broadened red wing. Adding in a second narrow line at $E = 7.06_{-0.02}^{+0.02}$ keV ($EW = 20_{-0}^{+0}$ eV), representing a contribution from Fe K β emission (and so a flux of $0.16\times$ that of K α), resulted in a marginal statistical improvement in fit ($\Delta\chi^2/\Delta\nu = -8/-2$), though the visual improvement in fit was readily apparent. Attempting to model the remaining residual feature with a single broad line produced unsatisfactory results, however. As such, we added a third narrow Gaussian line at $6.78_{-0.05}^{+0.06}$ keV ($EW = 29_{-9}^{+18}$ eV), representing ionized iron, which further improved the fit by $\Delta\chi^2/\Delta\nu = -7/-2$. While both the ionized iron line and Fe K β line did not result in statistically significant improvements in fit, according to the F -test, they nonetheless produced substantial visual improvements to the fit and nicely modeled the residual features that could not be accounted for by a broad Fe K α line component. A residual emission line-like feature remains around ~ 7.1 keV in the observed frame, which likely represents a line from Ni X-XVI, but adding in an additional Gaussian to model it results in no net improvement in fit so it is left unmodeled.

It should be noted that Gondoin et al. did not report the detection of a broad Fe K α line in their analysis, and that our attempts to include one show that, while the inclusion of a broad component at 6.40 keV does improve our fit by $\Delta\chi^2/\Delta\nu = -13/-2$, a relativistic disk line model such as `diskline` or `laor` shows no improvement over a simple Gaussian with $\sigma = 0.16 \pm 0.11$ keV. Further, the parameter values of the `diskline` and `laor` components are largely unconstrained, as one might expect. Even so, our best statistical fit was achieved with a `rdblur(reflion)` model, albeit with the emissivity index and inclination angle of the disk unconstrained. The inner radius of disk emission was constrained to $r_{\min} \leq 29 r_g$.

Best-fit values and error bars for all the parameters in this model are listed in Table 9. Fig. 8 shows the iron line residual, best fit to this residual, and relative contributions of the individual model components, respectively. The `diskline` and `laor` fits are shown in Table 10, while comparisons of the ionized disk reflection spectrum with and without relativistic smearing can be found in Table 11.

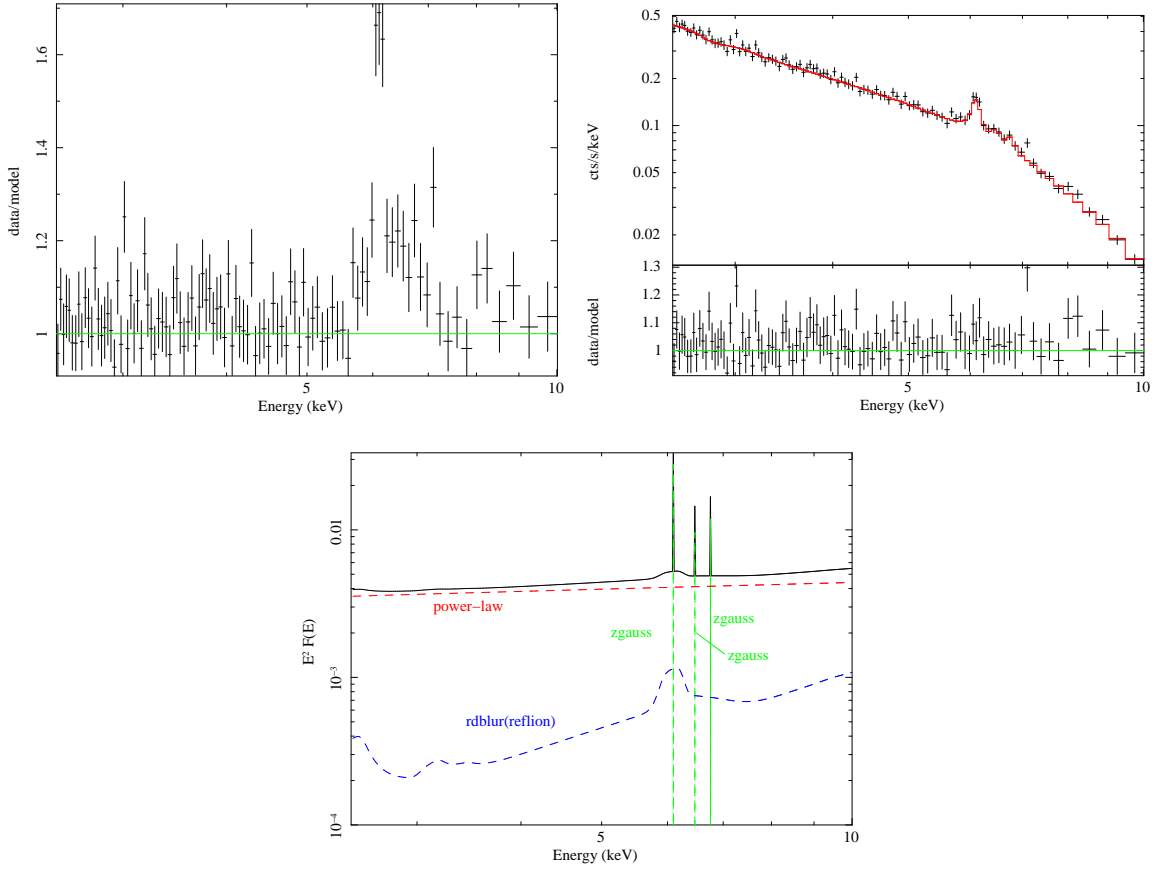


Fig. 8.— *Top left:* The 2.5 – 10.0 keV spectrum of Fairall 9 fit with a continuum composed of a power-law model modified by Galactic photoabsorption and a blackbody soft excess. $\chi^2/\nu = 816/699$ (1.17). *Top right:* The 2.5 – 10.0 keV best-fit model for Fairall 9, including our continuum model and an ionized disk reflection spectrum convolved with the `rdblur` relativistic smearing kernel. $\chi^2/\nu = 679/691$ (0.98). *Bottom:* An $E^2 F(E)$ plot depicting the relative flux in each of the model components in the spectrum.

Model Component	Parameter	Value
phabs	N_{H} (cm^{-2})	3.19×10^{20}
zpo	Γ_{po}	$1.88^{+0.20}_{-0.04}$
	flux ($\text{ph cm}^{-2} \text{s}^{-1}$)	$3.54^{+0.96}_{-0.41} \times 10^{-3}$
zgauss	E (keV)	$6.40^{+0.01}_{-0.02}$
	flux ($\text{ph cm}^{-2} \text{s}^{-1}$)	$1.54^{+0.27}_{-0.27} \times 10^{-5}$
	EW (eV)	115^{+20}_{-20}
zgauss	E (keV)	$6.78^{+0.06}_{-0.05}$
	flux ($\text{ph cm}^{-2} \text{s}^{-1}$)	$3.72^{+2.36}_{-2.38} \times 10^{-6}$
	EW (eV)	29^{+18}_{-19}
zgauss	E (keV)	$7.06^{+0.02}_{-0.02}$
	flux ($\text{ph cm}^{-2} \text{s}^{-1}$)	$2.47^{+0.00}_{-0.00} \times 10^{-6}$
	EW (eV)	20^{+0}_{-0}
rdblur	α	$10.00^{+0.00}_{-10.00}$
	i ($^{\circ}$)	54^{+36}_{-54}
	r_{min} (r_{g})	$8.04^{+21}_{-8.04}$
	r_{max} (r_{g})	400
reflion	Fe/solar	$0.86^{+0.75}_{-0.48}$
	ξ_{refl} ($\text{erg cm}^{-1} \text{s}^{-1}$)	50^{+575}_{-50}
	Γ_{refl}	$1.88^{+0.20}_{-0.04}$
	R_{refl}	$0.70^{+7.00}_{-0.69}$
	flux ($\text{ph cm}^{-2} \text{s}^{-1}$)	$2.58^{+12.45}_{-2.04} \times 10^{-6}$
χ^2/ν		679/691 (0.98)

Table 9: Best-fitting model parameters for the 2.5 – 10.0 keV spectrum of Fairall 9, including components and parameter values from 0.6 – 1.5 keV for completeness. The energies from 1.5 – 2.5 keV were not included due to the presence of absorption edges from the *XMM-Newton* mirrors. Error bars are quoted at 90% confidence. We required the 6.4 keV **zgauss** line to be intrinsically narrow, i.e., $\sigma = 0$ keV. Redshifts were frozen at the cosmological value for the source, in this case $z = 0.0470$. A warm absorber is present in this object, as in many other Sy 1 sources.

5. Results

We have compiled the relevant parameter constraints from all of our spectral fits to eight Sy 1 sources: MCG–5-23-16, Mrk 766, NGC 3783, NGC 4051, Ark 120, Fairall 9, NGC 2992, and 3C 273. Table 10 presents the results of fitting the broad iron line with a simple `diskline` or `laor` model as a first approximation. Table 11 displays the results of fitting a more detailed, physical model consisting of many reflection features from the accretion disk as a whole, both with and without relativistic smearing via `rdblur` and `kdblur`. Note that, for nearly every source, a model including reflection from an ionized disk convolved with a relativistic smearing kernel provides the best statistical fit, as judged by the change in chi-squared per additional degree of freedom in the model (i.e., the F -test), tightness of the parameter constraints and reduction in the residuals from the data/model ratio.

Previous studies have indicated that broad iron lines may be present in up to 42% of AGN observed with the *XMM-Newton*/EPIC-pn camera that have $\gtrsim 10^4$ counts (Guainazzi et al. 2006). To assess whether evidence exists for a relativistically broadened iron line in each of our data sets, we first considered the `diskline` and `laor` fits in which BH spin is fixed at $a = 0.0$ and $a = 0.998$, respectively. While each source demonstrated a significant improvement in its global fit as compared to a model fitting only a narrow iron line core with a Gaussian component, the most important parameter to evaluate in this case is the inner radius of disk emission. Roughly speaking, as stated in §3.2, if $r_{\min} \lesssim 20 r_g$ we can say with some confidence that there is substantial emission from the inner part of the accretion disk where relativistic effects (such as BH spin) become important in shaping the overall iron line profile. Out of our eight sources, Fairall 9 and Ark 120 had very poor constraints on r_{\min} based on their `diskline` and `laor` fits. Of the six sources where r_{\min} could be constrained, only MCG–5-23-16 did not show a substantial contribution from $r_{\min} \leq 20 r_g$, either in the `diskline` or `laor` fit. All of our sources showed little difference between the `diskline` and `laor` model fitting results, statistically, as judged by their reduced χ^2 values. The four sources that did show very modest reductions in reduced χ^2 with a `laor` model were MCG–5-23-16, Mrk 766, NGC 2992 and 3C 273. Of these, MCG–5-23-16 showed the most significant improvement in fit with `laor` as opposed to `diskline`, though it is doubtful that this difference represents evidence for a spinning BH, given the constraint on the inner disk radius in this source.

We have also examined the question of how robust the presence of a broad line is in the spectrum when reflection is included. Beginning with a base continuum model including a static ionized disk reflection spectrum (Ross & Fabian 2005), we noted the overall goodness-of-fit and the residual features remaining, especially around the iron line region. We then convolved this model with relativistic effects, first using the `rdblur` smearing kernel, then

substituting in `kdblur` (Table 3). Due to the nature of the BH spin parameter space, the difference between an $a = 0.8$ and an $a = 0.998$ BH is much more pronounced than the difference between an $a = 0.0$ and an $a = 0.8$ BH. Therefore, while a significant improvement in the global fit with either model indicates that relativistic smearing is important in the system, further significant improvement with `kdblur` instead of `rdblur` suggests that not only is relativity important, but in the best-fit scenario the BH spin likely tends toward the maximum theoretical value.

The `rdblur` and `kdblur` fits were at least as good or better than the `diskline` and `laor` model fits in each source. The difference is greatest in the cases of MCG–5-23-16 and NGC 4051. These smearing models also returned similar results in terms of parameter constraints and overall fit to the iron line profile in each source, and in nearly all cases also produced an improvement in the overall goodness-of-fit over the non-smearred case. More marginal improvements were seen in Fairall 9, NGC 2992 and 3C 273; not coincidentally, these are the three sources for which we have the lowest photon count (each has $\leq 4 \times 10^5$ photons from 2–10 keV). Note that it was also difficult to constrain several other parameters in these AGN: the emissivity index and inner radius of disk emission, particularly, and in the case of Fairall 9 even the inclination angle of the disk to our line of sight. Normally inclination is well-constrained by the position of the blue wing of the Fe $K\alpha$ line profile, but Fairall 9 has the fewest counts of any of our sources, and so the blue wing cannot easily be separated from the underlying continuum. This underscores the importance of photon statistics in evaluating the relevance of relativistic effects in an AGN spectrum. Out of the five sources that showed significant improvement with relativistic smearing, none showed a significant statistical preference for either `rdblur` or `kdblur` according to their reduced chi-squared values, implying that we are not able to robustly distinguish between a non-spinning and a rapidly-spinning BH in any of our sample members. MCG–5-23-16, Ark 120, NGC 2992 and 3C 273 all show a modest preference for `kdblur` over `rdblur`, while NGC 3783 shows the opposite. The other sources show equally good fits to each model.

We note that the `reflion` model (Ross & Fabian 2005) does not include a formal parameter for the reflection fraction of the disk, so in order to facilitate comparison between our results and those from studies using other models to parameterize reflection (e.g., `pexrav`, Magdziarz & Zdziarski (1995)), we have estimated R_{refl} in all of our models shown in Table 11 and in §4. To make these estimates, we have assumed that for $R_{\text{refl}} = 1$, half of the radiation from the hard X-ray power-law is received and reflected by the disk, with the other half traveling directly to the observer. Reflection fractions of greater than unity then indicate that more than half of the power-law radiation illuminates the disk, implying anisotropic emission from the power-law source or perhaps strong light-bending of this emission near

the BH. Operationally, we compute R_{refl} using the following formula:

$$R_{\text{refl}} = \frac{N_{\text{refl}}}{N_{\text{po}}} \frac{F_{\text{refl}}}{F_{\text{po}}} \left(\frac{\xi}{30} \right)^{-1}. \quad (1)$$

Here N_{refl} and N_{po} denote the normalizations of the `reflion` and power-law components from our best-fit spectral model, (ξ) is the best-fit ionization parameter characterizing the disk reflection, and F_{refl} and F_{po} are the total fluxes contained in the `reflion` and power-law components for unity normalization over the full wavelength range (0.001 – 1000 keV). These reflection fractions are often poorly constrained due to the lack of simultaneous high energy data above 10 keV, which would enable us to constrain the amount of reflection (as well as the iron abundance and ionization of the disk) more effectively by measuring the Compton hump, which typically peaks at 20 – 30 keV. Having this high energy data would therefore allow us better parameterize many properties of the disk, enabling better constraints on the nature of the spacetime surrounding the BH (e.g., r_{min} and the BH spin). For this reason, part II of this work will utilize *Suzaku*/XIS+HXD data to establish robust BH spin constraints in these AGN.

AGN	α	i ($^\circ$)	r_{\min} (r_g)	χ^2/ν
MCG-5-23-16	1.35 – 3.04	29 – 42	≤ 66	1513/1490 (1.02)
	1.98 – 4.30	21 – 37	18 – 44	1509/1490 (1.01)
Mrk 766	2.50 – 3.84	10 – 31	≤ 11	1423/1309 (1.09)
	---	58 – 72	1.92 – 2.78	1421/1309 (1.09)
NGC 3783	1.94 – 1.96	21 – 23	≤ 18	1478/1489 (0.99)
	1.38 – 2.87	21 – 24	≤ 25	1485/1489 (1.00)
NGC 4051	≤ 6.76	12 – 52	≤ 567	1528/1398 (1.09)
	2.45 – 3.63	15 – 45	3.96 – 6.98	1528/1398 (1.09)
Fairall 9	---	≤ 50	---	685/695 (0.99)
	---	≤ 46	---	688/695 (0.99)
Ark 120	≤ 1.98	31 – 51	≤ 174	1528/1419 (1.08)
	---	50 – 72	---	1528/1419 (1.08)
NGC 2992	1.34 – 4.77	44 – 62	≤ 23	1400/1311 (1.07)
	1.60 – 2.74	45 – 63	≤ 19	1399/1311 (1.07)
3C 273	≤ 2.97	22 – 62	9 – 38	231/265 (0.87)
	---	53 – 82	≤ 15	228/265 (0.86)

Table 10: Comparison of the spectral fitting results for the 2.5 – 10.0 keV spectra using the `diskline` and `laor` models. For each source the top row represents the `diskline` range in parameter value while the bottom row represents the `laor` range in parameter value. Ranges are given at 90% confidence. A dashed line rather than a numerical value indicates that the parameter could not be statistically constrained in a formal error analysis.

AGN	Fe/solar	ξ_{refl} (erg cm $^{-1}$ s $^{-1}$)	R_{refl}	α	i ($^{\circ}$)	r_{min} (r_g)	χ^2/ν
MCG 5-23-16	0.53 – 0.83	≤ 34	0.33 – 0.50				1555/1492 (1.04)
	0.49 – 0.70	≤ 31	0.33 – 0.44	1.05 – 3.13	23 – 40	≤ 69	1492/1488 (1.00)
	0.56 – 0.64	≤ 31	0.39 – 0.43	1.05 – 4.40	22 – 37	≤ 64	1485/1488 (1.00)
Mrk 766	0.65 – 4.11	1506 – 5146	≤ 0.01				1436/1311 (1.10)
	---	509 – 2866	≤ 0.14	1.74 – 3.25	25 – 32	≤ 17	1426/1308 (1.09)
	---	495 – 1290	≤ 0.18	1.84 – 3.64	23 – 32	≤ 14	1426/1308 (1.09)
NGC 3783	0.99 – 1.87	33 – 72	0.22 – 0.61				1497/1490 (1.00)
	0.71 – 1.71	≤ 54	0.12 – 0.71	1.03 – 3.31	21 – 26	≤ 46	1480/1487 (1.00)
	0.70 – 1.67	≤ 57	0.12 – 0.70	≤ 4.50	20 – 26	≤ 44	1486/1487 (1.00)
NGC 4051	≤ 0.18	133 – 847	0.06 – 2.25				1485/1395 (1.06)
	0.18 – 0.70	37 – 120	0.43 – 24.53	---	26 – 38	≤ 7.84	1468/1392 (1.05)
	0.34 – 0.62	38 – 125	0.45 – 13.82	---	23 – 39	3.99 – 9.35	1468/1392 (1.05)
Fairall 9	≤ 1.75	331 – 2212	≤ 0.10				684/696 (0.98)
	0.38 – 1.61	≤ 625	0.01 – 7.70	---	---	≤ 29	679/692 (0.98)
	0.28 – 2.37	50 – 2684	≤ 12.94	---	---	---	679/692 (0.98)
Ark 120	0.93 – 1.60	117 – 164	0.13 – 0.31				1576/1423 (1.11)
	0.42 – 0.68	≤ 35	0.85 – 2.42	≤ 1.93	35 – 57	≤ 80	1511/1418 (1.07)
	0.42 – 0.65	≤ 38	0.69 – 2.07	---	50 – 55	---	1509/1418 (1.07)
NGC 2992	0.66 – 6.06	≤ 226	≤ 0.35				1412/1313 (1.08)
	---	≤ 310	0.21 – 0.39	≤ 3.00	10 – 27	≤ 304	1398/1310 (1.07)
	---	≤ 67	0.12 – 0.59	---	33 – 47	2.91 – 4.93	1396/1310 (1.07)
3C 273	---	206 – 394	0.02 – 0.30				236/267 (0.88)
	---	≤ 1769	0.01 – 16.75	≤ 2.57	30 – 44	≤ 21	232/264 (0.88)
	---	≤ 5689	---	3.97 – 9.98	35 – 73	≤ 3.73	229/264 (0.87)

Table 11: Comparison of the spectral fitting results for the 2.5 – 10.0 keV spectra using the ionized reflection model `reflion`, `rdblur(reflion)` and `kdblur(reflion)`. The latter two models convolve the reflection spectrum with smearing kernels from a non-spinning and maximally-spinning BH, respectively. For each column of data, the top row represents the `reflion` range in parameter values, the middle row shows the `rdblur(reflion)` values and the bottom row represents the `kdblur(reflion)` values. For the `reflion` component, the value of the incident power-law spectral index is set equal to that of the hard x-ray source. Reflection fraction is estimated as described above in the text, based on the relative fluxes and normalizations of the power-law and `reflion` components of this best-fit model. Parameter value ranges are given at 90% confidence.

6. Discussion and Conclusions

This paper explores the use of broad iron emission lines to constrain the importance of relativistic effects in a sample of AGN. Following our previous work on MCG–6-30-15 (BR06), this study of an additional eight prominent Sy 1 AGN observed to have prominent iron lines has provided us with some intriguing data on this subject and has also put us in an excellent position to apply our spectral fitting techniques to many other sources in the future.

Though this sample is far too small to allow us to draw any robust conclusions about the nature of the spacetime in the nuclei of Sy 1 galaxies as a whole, this work has allowed us to design a viable method for evaluating the presence of a broad iron line in the data and using a sequence of models to assess the importance of relativistic smearing in shaping the spectral features emitted from the accretion disk around the BH. We have determined that four out of our eight sources show improvement in their goodness-of-fit parameters when relativistic effects from the inner disk are taken into account (one more shows at least marginal improvement). Of these four, two show more improvement with a smearing model designed for a maximally-rotating BH than for a non-spinning BH, which may suggest that BH spin is non-zero in these objects.

Access to energies greater than the *XMM* limit of 10 keV will help to better constrain the disk parameters these sources, in turn allowing for constraints to ultimately be placed on BH spin. This endeavor will be the focus of our follow-up *Suzaku* work on these AGN.

Based on our *XMM* data analysis we have arrived at three important conclusions that we hope will inform subsequent broad iron line and BH spin surveys:

1. Guainazzi et al. (2006) found that the fraction of AGN displaying broad iron lines in *XMM-Newton*/EPIC data increases dramatically when the spectra have more than $\sim 10^4$ counts. We find that EPIC spectra with $\sim 10^6$ counts are required in order to use these iron lines to assess the importance of relativistic effects in these sources.
2. Five out of nine sources from our broad Fe K line sample (including previous work on MCG–6-30-15) showed a significant improvement in their global goodness-of-fit when relativistic smearing was added to a static ionized disk reflection spectrum.
3. Though the *XMM-Newton*/EPIC-pn instrument allows us to resolve the broad iron line in excellent detail, its 10 keV energy cutoff limits our ability to accurately model the disk reflection continuum due to its inability to measure the peak energy of the Compton reflection hump at $\sim 20 - 30$ keV.

Further progress in this direction needs more data with newer, more sensitive, broader bandwidth instruments in order to provide constraints on BH spin. *Suzaku*, with its enhanced spectral resolution in the XIS detector and the HXD/PIN detector simultaneously covering the energy range from 10 – 60 keV, provides great advantages for this type of study. Part II of this work (forthcoming) will analyze archival *Suzaku* observations of these sources, enabling us to measure the peak of the Compton hump and break the degeneracies between the parameters of the disk and those governing the spacetime near the BH. *Suzaku* data will therefore allow us to constrain BH spin using our `kerrdisk` and `kerrconv` models.

Acknowledgements

We gratefully acknowledge the guidance and support of the University of Maryland at College Park’s Astronomy Department. Helpful contributions and advice for this work were imparted by LB’s dissertation defense committee: R. Mushotzky, S. McGaugh, S. Veilleux, M. C. Miller, and T. Jacobson. We are also indebted to Andy Fabian for his insightful comments that improved this work, and to the anonymous referee, who provided several recommendations which have helped us to focus this manuscript. LB also thanks the NASA Postdoctoral Program, administered by ORAU, for her current support at NASA’s GSFC. CSR gratefully acknowledges support from the National Science Foundation (grant AST 06-07428), as well as the U.Maryland/NASA-Goddard Center for Research and Exploration on Space Science and Technology (CRESST).

REFERENCES

- Balestra, I., Bianchi, S., & Matt, G. 2004, *Astr. Astrophys.*, 415, 437
- Ballantyne, D. R., Fabian, A. C., & Iwasawa, K. 2004, *Mon. Not. R. astr. Soc.*, 354, 839
- Behar, E., Rasmussen, A. P., Blustin, A. J., Sako, M., Kahn, S. M., Kaastra, J. S., Branduardi-Raymont, G., & Steenbrugge, K. C. 2003, *Astrophys. J.*, 598, 232
- Bevington, P. R. 1969, *Data reduction and error analysis for the physical sciences* (New York: McGraw-Hill, 1969)
- Blustin, A. J., Branduardi-Raymont, G., Behar, E., Kaastra, J. S., Kahn, S. M., Page, M. J., Sako, M., & Steenbrugge, K. C. 2002, *Astr. Astrophys.*, 392, 453

- Braitto, V., Reeves, J. N., Dewangan, G., George, I., Griffiths, R., Markowitz, A., Nandra, K., Porquet, D., Ptak, A., Turner, T. J., Yaqoob, T., & Weaver, K. 2006, *Astronomische Nachrichten*, 327, 1067
- Brandt, W. N., Fabian, A. C., Nandra, K., & Tsuruta, S. 1993, *Mon. Not. R. astr. Soc.*, 265, 996
- Brenneman, L. W. & Reynolds, C. S. 2006, *Astrophys. J.*, 652, 1028
- Brenneman, L. W., Reynolds, C. S., Wilms, J., & Kaiser, M. E. 2007, *Astrophys. J.*, 666, 817
- Brenneman, L. W., Weaver, K. A., Kadler, M., Tueller, J., Marscher, A., Ros, E., Zensus, A., Kovalev, Y. Y., Aller, M., Aller, H., Irwin, J., Kerp, J., & Kaufmann, S. 2009, *Astrophys. J.*, 698, 528
- Crenshaw, D. M. & Kraemer, S. B. 2001, *Astrophys. J. Lett.*, 562, L29
- Crenshaw, D. M., Kraemer, S. B., Boggess, A., Maran, S. P., Mushotzky, R. F., & Wu, C.-C. 1999, *Astrophys. J.*, 516, 750
- Dewangan, G. C., Griffiths, R. E., & Schurch, N. J. 2003, *Astrophys. J.*, 592, 52
- Dickey, J. M. & Lockman, F. J. 1990, *ARA&A*, 28, 215
- Dovčiak, M., Karas, V., & Yaqoob, T. 2004, *Astrophys. J. Suppl.*, 153, 205
- Fabian, A. C., Rees, M. J., Stella, L., & White, N. 1989, *Mon. Not. R. astr. Soc.*, 238, 729
- Fabian, A. C., Vaughan, S., Nandra, K., Iwasawa, K., Ballantyne, D. R., Lee, J. C., de Rosa, A., Turner, A., & Young, A. J. 2002, *Mon. Not. R. astr. Soc.*, 335, L1
- George, I. M., Turner, T. J., Mushotzky, R., Nandra, K., & Netzer, H. 1998, *Astrophys. J.*, 503, 174
- George, I. M., Turner, T. J., & Netzer, H. 1995, *Astrophys. J. Lett.*, 438, L67
- Gilli, R., Maiolino, R., Marconi, A., Risaliti, G., Dadina, M., Weaver, K. A., & Colbert, E. J. M. 2000, *Astr. Astrophys.*, 355, 485
- Gondoin, P., Lumb, D., Siddiqui, H., Guainazzi, M., & Schartel, N. 2001, *Astr. Astrophys.*, 373, 805
- Guainazzi, M., Bianchi, S., & Dovčiak, M. 2006, *Astronomische Nachrichten*, 327, 1032

- Guainazzi, M., Mihara, T., Otani, C., & Matsuoka, M. 1996, *Publ. astr. Soc. Japan*, 48, 781
- Haardt, F., Fossati, G., Grandi, P., Celotti, A., Pian, E., Ghisellini, G., Malizia, A., Maraschi, L., Paciesas, W., Raiteri, C. M., Tagliaferri, G., Treves, A., Urry, C. M., Villata, M., & Wagner, S. 1998, *Astr. Astrophys.*, 340, 35
- Jansen, F., Lumb, D., Altieri, B., Clavel, J., Ehle, M., Erd, C., Gabriel, C., Guainazzi, M., Gondoin, P., Much, R., Munoz, R., Santos, M., Schartel, N., Texier, D., & Vacanti, G. 2001, *Astr. Astrophys.*, 365, L1
- Kalberla, P. M. W., Burton, W. B., Hartmann, D., Arnal, E. M., Bajaja, E., Morras, R., & Pöppel, W. G. L. 2005, *Astr. Astrophys.*, 440, 775
- Kaspi, S., Brandt, W. N., George, I. M., Netzer, H., Crenshaw, D. M., Gabel, J. R., Hamann, F. W., Kaiser, M. E., Koratkar, A., Kraemer, S. B., Kriss, G. A., Mathur, S., Mushotzky, R. F., Nandra, K., Peterson, B. M., Shields, J. C., Turner, T. J., & Zheng, W. 2002, *Astrophys. J.*, 574, 643
- Kaspi, S., Brandt, W. N., Netzer, H., George, I. M., Chartas, G., Behar, E., Sambruna, R. M., Garmire, G. P., & Nousek, J. A. 2001, *Astrophys. J.*, 554, 216
- Kaspi, S., Brandt, W. N., Netzer, H., Sambruna, R., Chartas, G., Garmire, G. P., & Nousek, J. A. 2000, *Astrophys. J. Lett.*, 535, L17
- Kataoka, J., Tanihata, C., Kawai, N., Takahara, F., Takahashi, T., Edwards, P. G., & Makino, F. 2002, *Mon. Not. R. astr. Soc.*, 336, 932
- Lamer, G., McHardy, I. M., Uttley, P., & Jahoda, K. 2003, *Mon. Not. R. astr. Soc.*, 338, 323
- Laor, A. 1991, *Astrophys. J.*, 376, 90
- Leighly, K. M., Mushotzky, R. F., Yaqoob, T., Kunieda, H., & Edelson, R. 1996, *Astrophys. J.*, 469, 147
- Magdziarz, P. & Zdziarski, A. A. 1995, *Mon. Not. R. astr. Soc.*, 273, 837
- Mason, K. O., Branduardi-Raymont, G., Ogle, P. M., Page, M. J., Puchnarewicz, E. M., Behar, E., Córdova, F. A., Davis, S., Maraschi, L., McHardy, I. M., O’Brien, P. T., Priedhorsky, W. C., & Sasseen, T. P. 2003, *Astrophys. J.*, 582, 95
- Mason, K. O., McHardy, I. M., Page, M. J., Uttley, P., Córdova, F. A., Maraschi, L., Priedhorsky, W. C., Puchnarewicz, E. M., & Sasseen, T. 2002, *Astrophys. J. Lett.*, 580, L117

- Matt, G., Perola, G. C., Fiore, F., Guainazzi, M., Nicastro, F., & Piro, L. 2000, *Astr. Astrophys.*, 363, 863
- McHardy, I. M., Lawrence, A., Pye, J. P., & Pounds, K. A. 1981, *Mon. Not. R. astr. Soc.*, 197, 893
- Miller, J. M. 2007, ArXiv e-prints, 705
- Nandra, K., George, I. M., Mushotzky, R. F., Turner, T. J., & Yaqoob, T. 1997, *Astrophys. J.*, 476, 70
- Nandra, K., O’Neill, P. M., George, I. M., & Reeves, J. N. 2007, *MNRAS*, 382, 194
- Narayan, R., McClintock, J. E., & Shafee, R. 2007, ArXiv e-prints, 710
- Page, K. L., Turner, M. J. L., Done, C., O’Brien, P. T., Reeves, J. N., Sembay, S., & Stuhlinger, M. 2004, *Mon. Not. R. astr. Soc.*, 349, 57
- Piccinotti, G., Mushotzky, R. F., Boldt, E. A., Holt, S. S., Marshall, F. E., Serlemitsos, P. J., & Shafer, R. A. 1982, *Astrophys. J.*, 253, 485
- Ponti, G., Miniutti, G., Cappi, M., Maraschi, L., Fabian, A. C., & Iwasawa, K. 2006, *Mon. Not. R. astr. Soc.*, 368, 903
- Pounds, K. A., Nandra, K., Fink, H. H., & Makino, F. 1994, *Mon. Not. R. astr. Soc.*, 267, 193
- Pounds, K. A., Reeves, J. N., King, A. R., & Page, K. L. 2004, *Mon. Not. R. astr. Soc.*, 350, 10
- Pounds, K. A., Reeves, J. N., Page, K. L., Wynn, G. A., & O’Brien, P. T. 2003, *Mon. Not. R. astr. Soc.*, 342, 1147
- Reeves, J. N., Awaki, H., Dewangan, G. C., Fabian, A. C., Fukazawa, Y., Gallo, L., Griffiths, R., Inoue, H., Kunieda, H., Markowitz, A., Miniutti, G., Mizuno, T., Mushotzky, R., Okajima, T., Ptak, A., Takahashi, T., Terashima, Y., Ushio, M., Watanabe, S., Yamasaki, T., Yamauchi, M., & Yaqoob, T. 2007, *Publ. astr. Soc. Japan*, 59, 301
- Reeves, J. N., Fabian, A. C., Kataoka, J., Kunieda, H., Markowitz, A., Miniutti, G., Okajima, T., Serlemitsos, P., Takahashi, T., Terashima, Y., & Yaqoob, T. 2006, *Astronomische Nachrichten*, 327, 1079
- Reeves, J. N., Nandra, K., George, I. M., Pounds, K. A., Turner, T. J., & Yaqoob, T. 2004, *Astrophys. J.*, 602, 648

- Reynolds, C. S. 1997, *Mon. Not. R. astr. Soc.*, 236, 513
- Reynolds, C. S. & Fabian, A. C. 2008, *Astrophys. J.*, 675, 1048
- Reynolds, C. S. & Nowak, M. A. 2003, *Phys. Reports*, 377, 389
- Ross, R. R. & Fabian, A. C. 2005, *Mon. Not. R. astr. Soc.*, 358, 211
- Ross, R. R., Fabian, A. C., & Brandt, W. N. 1996, *Mon. Not. R. astr. Soc.*, 278, 1082
- Schurch, N. J., Warwick, R. S., Griffiths, R. E., & Kahn, S. M. 2004, *Mon. Not. R. astr. Soc.*, 350, 1
- Türler, M., Chernyakova, M., Courvoisier, T. J.-L., Foellmi, C., Aller, M. F., Aller, H. D., Kraus, A., Krichbaum, T. P., Lähteenmäki, A., Marscher, A., McHardy, I. M., O'Brien, P. T., Page, K. L., Popescu, L., Robson, E. I., Tornikoski, M., & Ungerechts, H. 2006, *Astr. Astrophys.*, 451, L1
- Turner, M. J. L., Williams, O. R., Courvoisier, T. J. L., Stewart, G. C., Nandra, K., Pounds, K. A., Ohashi, T., Makishima, K., Inoue, H., Kii, T., Makino, F., Hayashida, K., Tanaka, Y., Takano, S., & Koyama, K. 1990, *Mon. Not. R. astr. Soc.*, 244, 310
- Turner, T. J., Kraemer, S. B., George, I. M., Reeves, J. N., & Bottorff, M. C. 2005, *Astrophys. J.*, 618, 155
- Turner, T. J., Miller, L., George, I. M., & Reeves, J. N. 2006, *Astr. Astrophys.*, 445, 59
- Turner, T. J., Nandra, K., George, I. M., Fabian, A. C., & Pounds, K. A. 1993, *Astrophys. J.*, 419, 127
- Turner, T. J. & Pounds, K. A. 1989, *Mon. Not. R. astr. Soc.*, 240, 833
- Uttley, P., Fruscione, A., McHardy, I., & Lamer, G. 2003, *Astrophys. J.*, 595, 656
- Uttley, P., Taylor, R. D., McHardy, I. M., Page, M. J., Mason, K. O., Lamer, G., & Fruscione, A. 2004, *Mon. Not. R. astr. Soc.*, 347, 1345
- Vaughan, S., Fabian, A. C., Ballantyne, D. R., De Rosa, A., Piro, L., & Matt, G. 2004, *Mon. Not. R. astr. Soc.*, 351, 193
- Ward, M., Elvis, M., Fabbiano, G., Carleton, N. P., Willner, S. P., & Lawrence, A. 1987, *Astrophys. J.*, 315, 74
- Weaver, K. A., Krolik, J. H., & Pier, E. A. 1998, *Astrophys. J.*, 498, 213

Weaver, K. A., Yaqoob, T., Mushotzky, R. F., Nousek, J., Hayashi, I., & Koyama, K. 1997, *Astrophys. J.*, 474, 675

Yaqoob, T. & Serlemitsos, P. 2000, *Astrophys. J. Lett.*, 544, L95